Cell

Hindbrain Double-Negative Feedback Mediates Palatability-Guided Food and Water Consumption

Graphical Abstract

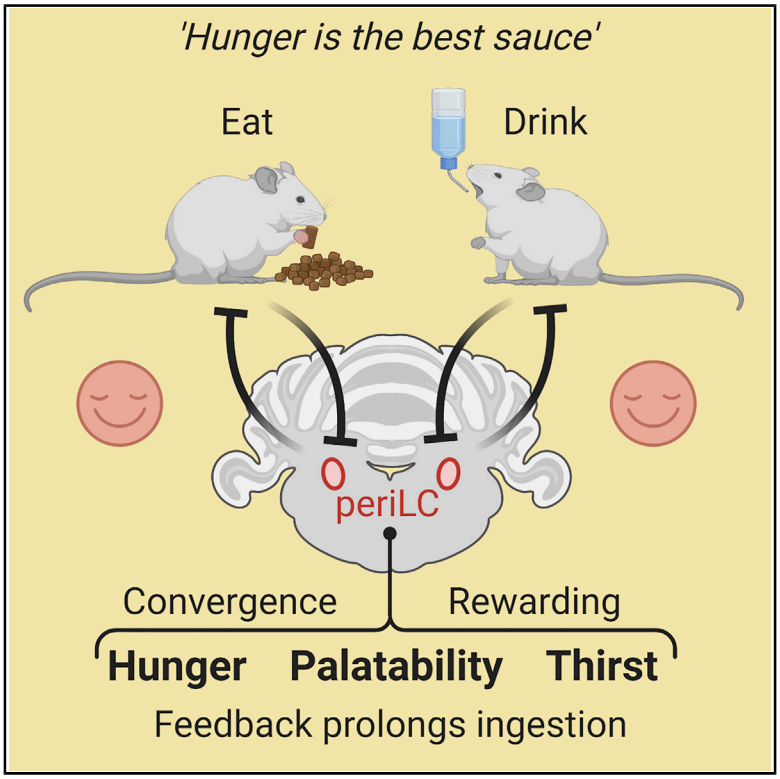

Authors

Rong Gong, Shengjin Xu, Ann Hermundstad, Yang Yu, Scott M. Sternson

Correspondence

sternsons@janelia.hhmi.org

In Brief

A subset of neurons in the hindbrain modulate palatability-driven hedonic eating.

Highlights

- PeriLC^{VGLUT2} neurons are a convergence point for hunger and thirst circuits
- Neuron responses to food or water intake are scaled by hunger, thirst, and palatability
- Consumption-triggered inhibition prolongs consumption and shifts taste preference
- PeriLC^{VGLUT2} neurons increase palatability, which promotes hedonic eating

Gong et al., 2020, Cell *182*, 1589–1605
September 17, 2020
https://doi.org/10.1016/j.cell.2020.07.031

CellPress

Cell

CellPress

Article

Hindbrain Double-Negative Feedback Mediates Palatability-Guided Food and Water Consumption

Rong Gong,[1] Shengjin Xu,[1] Ann Hermundstad,[1] Yang Yu,[2] and Scott M. Sternson[1,3,*]

[1]Janelia Research Campus, Howard Hughes Medical Institute, 19700 Helix Drive, Ashburn, VA 20147, USA

[2]Allen Institute, 615 Westlake Ave N, Seattle, WA 98109, USA

[3]Lead Contact

*Correspondence: sternsons@janelia.hhmi.org

https://doi.org/10.1016/j.cell.2020.07.031

SUMMARY

Hunger and thirst have distinct goals but control similar ingestive behaviors, and little is known about neural processes that are shared between these behavioral states. We identify glutamatergic neurons in the peri-locus coeruleus (periLC^{VGLUT2} neurons) as a polysynaptic convergence node from separate energy-sensitive and hydration-sensitive cell populations. We develop methods for stable hindbrain calcium imaging in free-moving mice, which show that periLC^{VGLUT2} neurons are tuned to ingestive behaviors and respond similarly to food or water consumption. PeriLC^{VGLUT2} neurons are scalably inhibited by palatability and homeostatic need during consumption. Inhibition of periLC^{VGLUT2} neurons is rewarding and increases consumption by enhancing palatability and prolonging ingestion duration. These properties comprise a double-negative feedback relationship that sustains food or water consumption without affecting food- or water-seeking. PeriLC^{VGLUT2} neurons are a hub between hunger and thirst that specifically controls motivation for food and water ingestion, which is a factor that contributes to hedonic overeating and obesity.

INTRODUCTION

Animal survival depends on neural mechanisms that motivate behaviors for fulfilling essential bodily needs. Classically, motivated behaviors can be deconstructed into three phases (Figure 1A; Craig, 1917). The preparatory (foraging) phase involves seeking and obtaining a desired outcome, often due to an accumulation of physiological need. This phase is followed by the consummatory phase, which includes sensory, motor, and reward processes associated with consummating the goal of the behavior (e.g., eating or drinking food or water). Satiety develops during the consummatory phase and eventually terminates the behavior, for example by PBN^{CGRP} neurons (Campos et al., 2016, 2018). Elucidating neural mechanisms for these motivated behaviors requires monitoring neuron dynamics to determine the selective involvement of neurons in the preparatory, consummatory, or satiety phases.

Agouti-related protein (AGRP) neurons in the hypothalamic arcuate nucleus (ARC) are activated by signals of energy deficit (Cowley et al., 2003). Artificial activation of AGRP neurons in sated mice induces virtual need states that mimic aspects of hunger by leading to food-directed foraging and selectively elicits avid food consumption (Figure 1A; Aponte et al., 2011; Krashes et al., 2011). AGRP neurons transmit negative valence, promote food seeking, and are rapidly inhibited when food is identified, such that activity is low during eating (Betley et al., 2015; Chen et al., 2015; Mandelblat-Cerf et al., 2015). Thus, AGRP neurons promote the preparatory phase of hunger, but they are not required for the consummatory phase of feeding behavior.

If AGRP neurons do not have a primary role in sustaining food consumption, then other neuron populations must be responsible for this function (Sternson and Eiselt, 2017). The rhythmic actions of ingestion are mediated by motor circuits in the hindbrain (Wiesenfeld et al., 1977), but control of ingestion and how long food is consumed are less well understood. Food palatability is associated with food pleasantness (hedonic value) and leads to a transition from ''sampling to savoring'' that prolongs bouts of consumption (Yeomans, 1998). In humans, hunger increases subjective reports of palatability (Cabanac, 1971). Easy access to low-cost, high-palatability food may also contribute to the rising incidence of obesity (Johnson and Wardle, 2014). Thus, palatability is a key factor controlling appetite (Sørensen et al., 2003), but little is known about the relationship between interoceptive sensory neurons and the neural circuits through which hunger shifts palatability and increases consumption.

Hunger is not the only state that influences ingestion. Thirst increases the ingestion of water by nitric oxide synthase 1 (Nos1)-expressing neurons in the supraformical organ (SFO^{NOS1}) that sense physiological dehydration, induce thirst-associated brain state changes, and selectively elicit water seeking (Allen et al.,

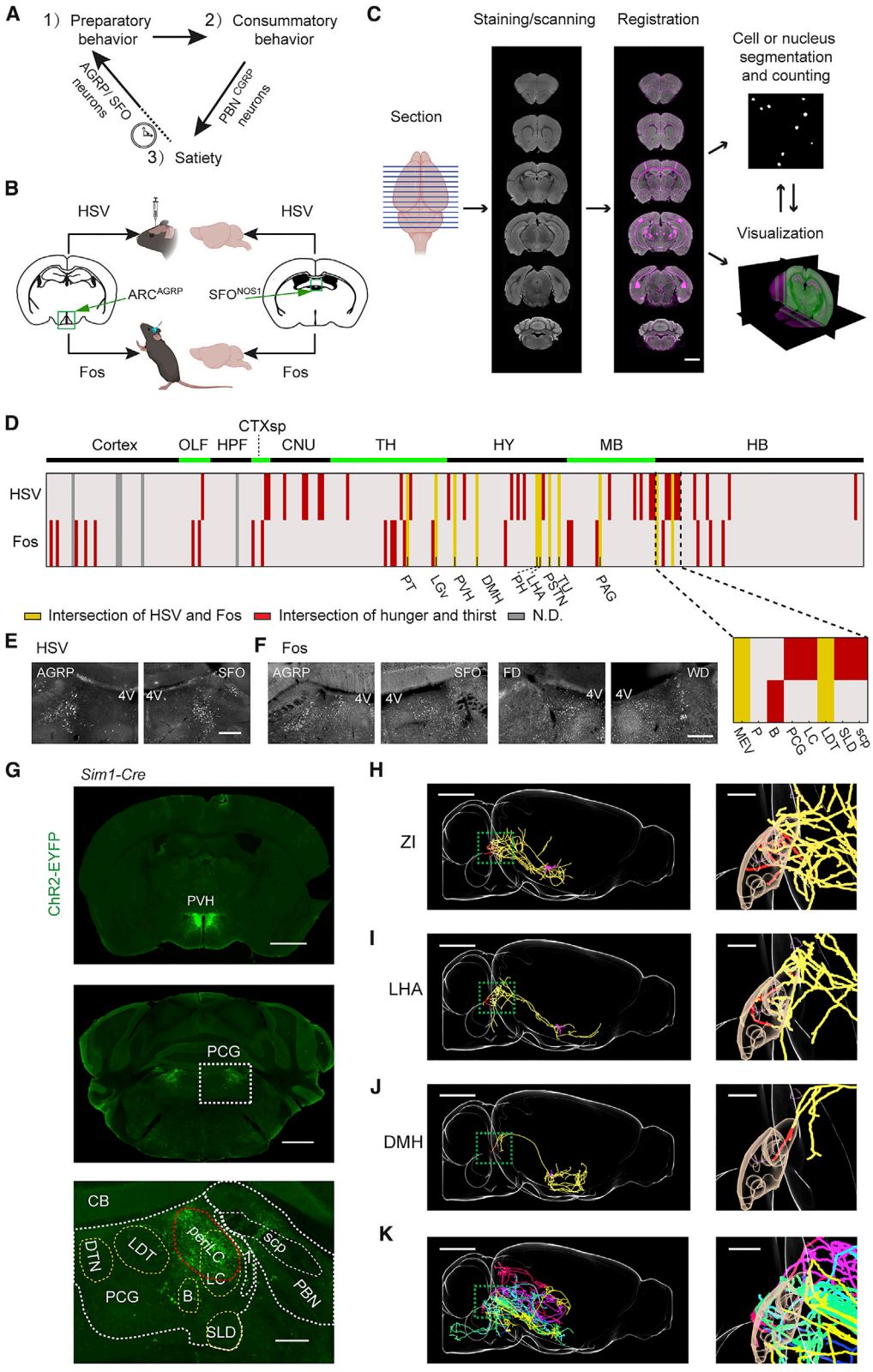

(legend on next page)

2019; Betley et al., 2015; Oka et al., 2015; Zimmerman et al., 2016). Hunger and thirst circuits involving AGRP neurons and SFO^{NOS1} neurons have been considered primarily as discrete interoceptive pathways for distinct physiological states. Less consideration has been given to the shared behavioral mechanisms between these different need states and the potential convergence of hunger and thirst circuits.

To investigate this knowledge gap, we leveraged the molecularly defined and separately localized AGRP and SFO^{NOS1} neurons as entry points to study the convergence of hunger and thirst circuits. We identified glutamatergic neurons in the anterior peri-locus coeruleus (periLC) as a polysynaptic convergence region in hunger and thirst behaviors. Circuit dynamics and causal perturbations show that periLC neurons control eating and drinking by regulating palatability during the consummatory phase of behavior.

RESULTS

Convergence of Feeding and Drinking Circuits

AGRP and SFO^{NOS1} neuron axon projections overlap in several downstream brain regions (Figure S1A). We hypothesized that feeding and drinking circuits converged at some points to mediate shared aspects of these behaviors. We developed a strategy to perform a broad search for anatomically defined and functionally important convergence points by using polysynaptic circuit mapping methods (Figure 1B). We looked for intersections of brain regions downstream of AGRP and SFO^{NOS1} neurons identified by Cre-dependent herpes simplex virus (HSV) anterograde polysynaptic labeling (Lo and Anderson, 2011) with the fluorescent protein tdTomato. We also performed Fos-mapping after optogenetic activation of AGRP neurons or SFO^{NOS1} neurons in the absence of food and water (Figures S1B and S1C) to identify downstream regions that are functionally activated in hunger and thirst. Brains from each group of mice were sectioned, stained, and registered to the Allen Institute Reference Brain Atlas, followed by image segmentation of labeled cells and nuclei and quantification of HSV-mediated tdTomato expression or Fos-immunoreactivity (IR) across multiple brain regions (Figure 1C; STAR Methods). Several subcortical areas contained both HSV-mediated tdTomato expression and Fos-IR, including some of the direct downstream projection targets of AGRP and SFO^{NOS1} neurons, such as paraventricular hypothalamic nucleus (PVH), lateral hypothalamic area (LHA), and paraventricular thalamus (PVT) (Figure 1D; Figures S1D–S1F), which have been previously emphasized as being crucial for different aspects of hunger and thirst behavior (Betley et al., 2013; Leib et al., 2017).

We were especially interested in whether this approach could identify poorly characterized brain areas involved in feeding and drinking, and we noticed a hotspot of HSV and Fos labeling within the hindbrain at the dorsolateral portion of the pontine central gray (PCG). In both AGRP and SFO^{NOS1} groups, we found similar labeling with HSV in the MEV (midbrain trigeminal nucleus), PCG, LC (locus coeruleus), LDT (laterodorsal tegmental area), SLD (sublaterodorsal tegmental area), and scp (superior cerebellar peduncles) (Figures 1D and 1E). Fos-IR was observed for both groups in the MEV, Barrington nucleus (B), and LDT (Figures 1D and 1F). We also found that cells in dorsolateral PCG showed elevated Fos in food-deprived (FD) mice or water-deprived (WD) mice but not in control mice (Figures 1F and S1G). In addition, we noted and a recent study reported (Li et al., 2019) that the PVH, which contains second-order neurons in hunger and thirst circuits (Atasoy et al., 2012; Leib et al., 2017), projects to the dorsolateral PCG (Figure 1G). This area has been defined anatomically as the periLC (Shipley et al., 1996) and includes the brain region surrounding the anterior portion of the LC that is flanked laterally by the MEV, medially by the LDT, and dorsally by the fourth ventricle (Figure 1G; see STAR Methods for explanation of anatomical terms). Single neuron reconstructions (Winnubst et al., 2019) showed inputs to PCG that originated from multiple brain areas associated with ingestive behaviors (Figures 1H–1K). Based on these results, we investigated the periLC and surrounding sites for a role in regulating food and water consumption.

PeriLC^{VGLUT2} Neurons in PCG Modulate Food Intake and Preference Learning

The periLC primarily contains glutamatergic (*Vglut2*-expressing) neurons, and they are flanked by GABAergic (*Vgat*-expressing) neurons in the LDT and tyrosine hydroxylase (TH)-expressing noradrenergic neurons in the LC (Figure S2A). Moreover, *Vglut2* is not expressed in LC noradrenergic neurons (Figure S2A). Based on our HSV experiments, we examined non-noradrenergic LC^{VGLUT2} and periLC^{VGLUT2} neurons (hereafter referred to as periLC^{VGLUT2} neurons) using chemogenetic and optogenetic perturbations during eating and drinking.

Chemogenetic inhibition of periLC^{VGLUT2} neurons by PSAM^{4}-GlyR and uPSEM^{792} (Magnus et al., 2019) in *ad-libitum*-fed and

Figure 1. Brain Mapping Downstream of AGRP or SFO^{NOS1} Neurons

(A) The three phases of motivated behavior.

(B) Intersectional strategy for anatomical (HSV) and functional (Fos) polysynaptic mapping of circuits downstream of AGRP or SFO^{NOS1} neurons.

(C) Pipeline for data acquisition and registration to the Allen Institute Mouse Brain Reference Atlas. Scale bar: 1 mm.

(D) Intersection of labeling from HSV or Fos mapping across AGRP groups and SFO^{NOS1} groups. Inset: 8 brain regions in and around the PCG. Red: anatomical or functional intersections. Yellow: four-way intersections. Gray: not determined. Abbreviations: see STAR Methods.

(E) HSV-tdTomato labeling in PCG. 4V: fourth ventricle. Scale bar: 500 μm.

(F) Fos-IR in PCG following AGRP or SFO^{NOS1} neuron activation, food deprivation (FD), or water deprivation (WD). Scale bar: 500 μm.

(G) ChR2-EYFP expression in PVH^{SIM1} neurons (top, scale bar: 2 mm) shows axon projections in the PCG (middle, scale bar: 1 mm), and overlapping periLC (bottom, scale bar: 250 μm).

(H) Sagittal view of a neuron in ZI projecting to PCG. Magenta: soma and dendrites. Red: axons in the MEV (magenta mask), B, PCG, LC, LDT, and SLD (brown mask). Yellow: axons in other regions. Scale bar: 2 mm. Inset: PCG, scale bar: 500 μm.

(I and J) The same as in (G) with neurons from DMH (I) and LHA (J).

(K) Overlay of six additional neurons projecting to PCG: LHA (green), HY (blue), LHA (yellow), LHA (purple), ZI (red), and AHN (lake blue).

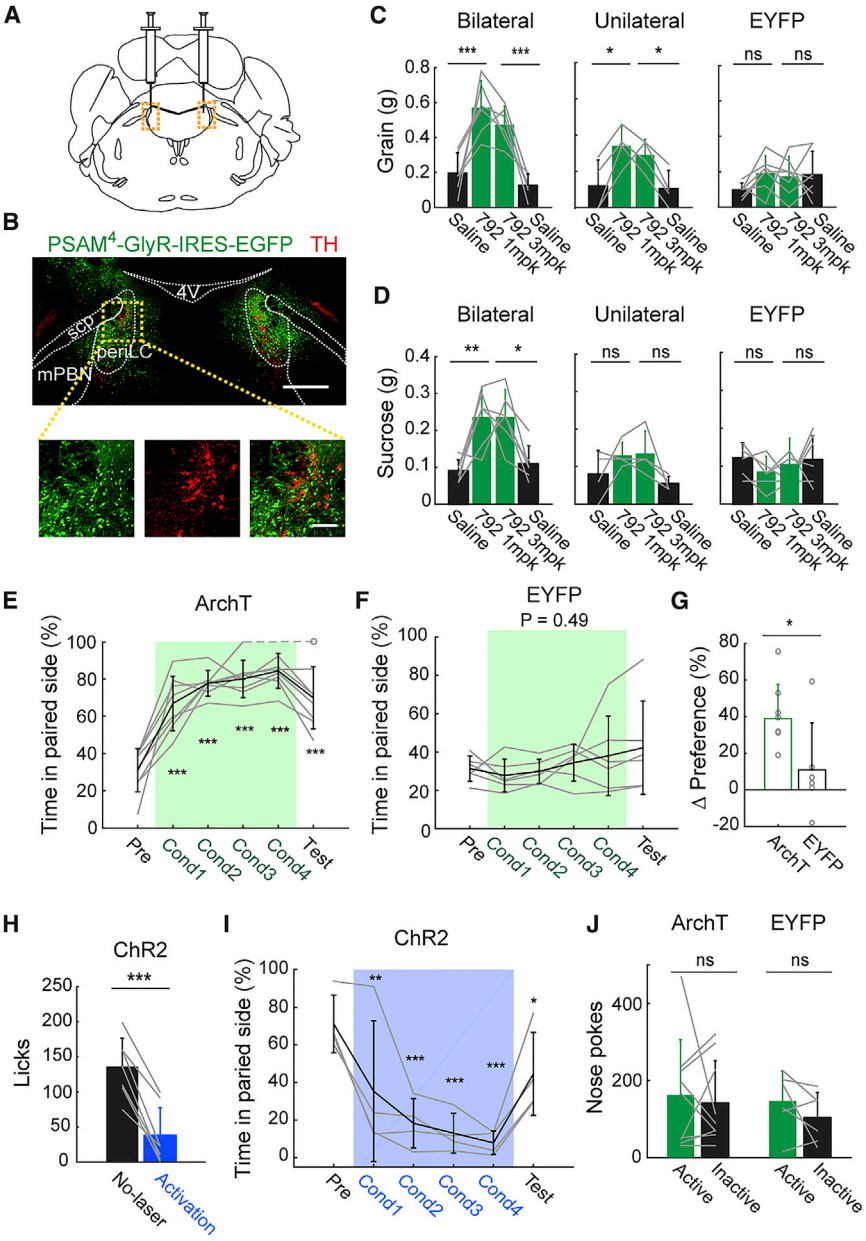

Figure 2. PeriLC^{VGLUT2} Neuron Inhibition Increases Appetite with Positive Valence

(A) Schematic of AAV targeting to periLC (boxes).

(B) PSAM^4-GlyR-IRES-EGFP expression (green) in periLC^{VGLUT2} neurons; scale bar: 500 μm. Insets: lack of co-expression with tyrosine hydroxylase (TH; red) neurons. Scale bar: 200 μm.

(C and D) Grain food pellet (C) or sucrose pellet (D) consumption (2 h) in mice with bilateral (n = 6, transduced neurons: 2838 ± 529) or unilateral (n = 4, transduced neurons: 946 ± 529) PSAM^4-GlyR expression and in EYFP (n = 7) control mice following saline or uPSEM^{792} injection.

(E and F) Percent time spent on the laser side for periLC^{VGLUT2} ArchT mice (E; n = 8) or EYFP mice (F; n = 6) before, during, and after photoinhibition conditioning. Pre, before conditioning; Cond1-Cond4, closed-loop place preference days 1–4; test, post-conditioning preference. Dashed gray line: skipped Cond4.

(G) Post-training change of occupancy time on the laser side for ArchT and EYFP control mice.

(H) Optogenetic activation of periLC^{VGLUT2} neurons decreases palatable food (Ensure) consumption (n = 7).

(I) Percent time spent on the laser side for periLC^{VGLUT2} ChR2 mice before, during, and after photoactivation conditioning (n = 4).

(J) Nose pokes at active and inactive ports in self-photoinhibition experiments for mice with periLC^{VGLUT2} neurons expressing ArchT (n = 9) or EYFP (n = 6). Error bars: SD. ns, $p > 0.05$; *$p < 0.05$; **$p < 0.01$; ***$p < 0.001$. Statistics: Table S1.

-hydrated mice significantly increased consumption of both grain food pellets and sugar pellets during the light period, which is a time during which mice normally eat little (Figures 2A–2D, S2B, and S2C; see STAR Methods). Chemogenetic inhibition of periLC^{VGLUT2} neurons did not reliably elicit water consumption (Figure S2D). Using a closed-loop place preference assay, we found that inhibition of periLC^{VGLUT2} neurons conditioned place preference that was sustained in a post-conditioning test in the absence of neuron activity perturbations, and this was not observed in enhanced yellow fluorescent protein (EYFP) control mice (Figures 2E–2G, S2E, and S2F). Optogenetic activation of periLC^{VGLUT2} neurons reduced food intake (Figure 2H) and elicited avoidance during closed-loop place preference (Figure 2I). These gain- or loss-of-function perturbations did not significantly alter locomotion or the number of entries to the light-paired side in archaerhodopsin-expressing (ArchT) mice or channelrhodopsin-2-expressing (ChR2) mice (Figures S2G–S2J). However, mice did not readily perform operant self-inhibition of periLC^{VGLUT2} neurons in a nose-poking task (Figure 2J), indicating that this cell population does not reinforce specific actions.

Taken together, these experiments show that inhibition of periLC^{VGLUT2} neurons increases food intake and is rewarding, whereas activation has the opposite effect. Notably, this is different than the AGRP neurons, which increase food seeking but mediate the unpleasant aspects of hunger (Betley et al., 2015).

Stable Imaging in the Hindbrain of Freely Moving Mice

To determine the natural dynamics of neurons in the PCG during motivated behavior, we developed an approach for *in vivo* calcium imaging of this brain region in freely moving mice during feeding and drinking by using a head-mounted miniature microscope and an implanted gradient index (GRIN) lens. Areas in the PCG are challenging targets for freely moving deep-brain calcium imaging because they are close to the cerebral ventricle, which is not stable during movement. Also, this area is overlaid

by the confluence of the transverse sinus and the sagittal sinus, which is critical for cerebral blood flow and damaging these blood vessels with the GRIN lens is fatal. We developed methods to mechanically displace the confluence during GRIN lens implantation (see STAR Methods), but we consistently observed large amplitude movement of brain tissue under the GRIN lens during locomotion or other activity (Figure 3A), which was incompatible with motion correction such that we were unable to detect reliable changes of individual neuronal calcium signals during behavior (Video S1).

We overcame this technical challenge by drawing inspiration from optrode recordings. We attached polyimide tubes to the GRIN lens through which we inserted tungsten wires to lock the underlying tissue into place (Figures 3B and S3A). The extended tungsten wires secured the imaging area and improved image stability. The recorded image time series was then suitable for small amplitude motion correction by using image registration (Figure 3B; Videos S2 and S3; see STAR Methods). This solution can benefit imaging deep brain targets that were previously unfeasible due to excessive brain movement.

PeriLC^{VGLUT2} Neurons Encode Consummatory Signals in Hunger and Thirst

We used *Vglut2* (*Slc17a6*)-*IRES-Cre* (Figure S3B) and *Gad2-IRES-Cre* mice with targeted Cre-dependent AAV injections to label glutamatergic neurons or GABAergic neurons, respectively, in the dorsolateral part of the PCG with GCaMP6f. PeriLC^{VGLUT2} neurons were modulated by consumption of food pellets or palatable liquid food (Ensure) (Figures S3C and S3D). These neurons were selective for consumption and were only weakly modulated by false food (wood block) or social interaction with the opposite sex (Figures S3C and S3D).

In contrast, *Gad2*-expressing inhibitory neurons, which were in the adjacent LDT (300 μm medial to periLC), were not selective for consumption and decreased activity when FD mice were presented with either a food pellet or a false food (Figure S3E). Further investigation indicated that a subset of LDT^{GAD2} neuron activity was increased during locomotion (Figure S3E, bottom), rearing, or grooming (Figure S3F). Our imaging results indicate that LDT Fos-IR (Figure 1D) was likely an indirect consequence of elevated foraging locomotor activity associated with activating AGRP and SFO^{NOS1} populations (Krashes et al., 2011). These results highlight the importance of temporally precise *in vivo* imaging over immediate early gene analysis to establish selective involvement in ingestive behaviors instead of indirect effects such as from locomotor activity. This also restricts consumption-modulated neurons to the periLC region.

Based on these observations, we focused on periLC^{VGLUT2} neurons across different phases of eating and drinking behavior (Figure 1A). We first investigated stimuli that are known to modulate AGRP neurons. To test the effect of hormonal signals of energy deficit, we injected ghrelin, which activates AGRP neurons within 2 min (Betley et al., 2015; Chen et al., 2015), but ghrelin did not significantly affect periLC^{VGLUT2} neuron activity (Figures S3G and S3H).

Next, we examined neural activity during cue-conditioned delivery of a small, fixed volume (3 μL) of palatable Ensure by using a motorized lick spout that was equipped with capacitive lick detection (Figure 3C; Video S4). In *ad-libitum*-fed mice, periLC^{VGLUT2} neurons showed responses during the consumption period (29% significantly inhibited, 25% significantly activated; Figures 3D and 3G). PeriLC^{VGLUT2} neurons also responded similarly during ingestion of moderate palatability liquid food by hungry mice (FD) (Figure 3E) as well as water consumption in a strong thirst state under water restriction (WR) (Figure 3F), with similar proportions of significantly modulated neurons under each condition (Figure 3G). Notably, many of the neurons that responded to food in hunger were also significantly modulated by water in thirst (Figure S3I; see STAR Methods). However, periLC^{VGLUT2} neurons were not modulated by the food-predictive auditory cue (Figures 3H and 3I). The lack of robust responding to a conditioned stimulus is different than that for AGRP neurons, which reduce their activity in the presence of food-predicting cues (Betley et al., 2015). Instead, the activated or inhibited neural responses of periLC^{VGLUT2} neurons were typically maintained throughout the consumption period (Figure 3J). These responses increased (or decreased) following the first lick and quickly reached a plateau (Figure 3K).

We also performed imaging during free-access, self-paced feeding trials without an auditory cue in which the food spout was always available. In these experiments, periLC^{VGLUT2} neurons were also most responsive during the consummatory phase (Figure S3J), but we did observe weak modulation during approach to the food spout (Figure S3J). This observation was most evident for the consumption-activated periLC^{VGLUT2} neurons, which showed a small decrease followed by an increase that preceded the first lick (Figure S3J, right). The mean response for consumption-inhibited periLC^{VGLUT2} neurons showed a slight increase during approach that decreased to the baseline level at the onset of the first lick, but these neurons were primarily modulated during consumption (Figure S3J). Thus, periLC^{VGLUT2} neuron responses were largest during consumption of both food and water, indicating that they are primarily involved in the consummatory phase of ingestive behaviors.

In addition, we considered a potential role for periLC^{VGLUT2} neurons in short-term termination of consumption. However, during free-access feeding bouts, we did not observe a systematic change in activity before or coinciding with cessation of consumption (Figure S3K).

Because periLC^{VGLUT2} neuron responses track consumption duration in cue-conditioned trials, we also examined the relationship of periLC^{VGLUT2} neuron responses to consumption duration in self-paced feeding bouts during free-access trials from energy deficit to satiety (Figure S3L). In this experiment, we interleaved cue-conditioned small-volume (3 μL) consumption trials for classification of periLC^{VGLUT2} neurons as "activated" or "inhibited" based on the same criteria used in Figure 3G (see STAR Methods). For most inhibited periLC^{VGLUT2} neurons (64%) and a smaller proportion of activated neurons (42%), the integrated response magnitude increased with consumption bout duration, which is expected for a response that persists during the consumption bout (Figures 3L–3N, S3M, and S3N). However, we found that 20% of the activated neurons had biphasic responses and became inhibited in the long duration bouts (Figures 3O and S3O). Thus, periLC^{VGLUT2} neurons, especially the inhibited

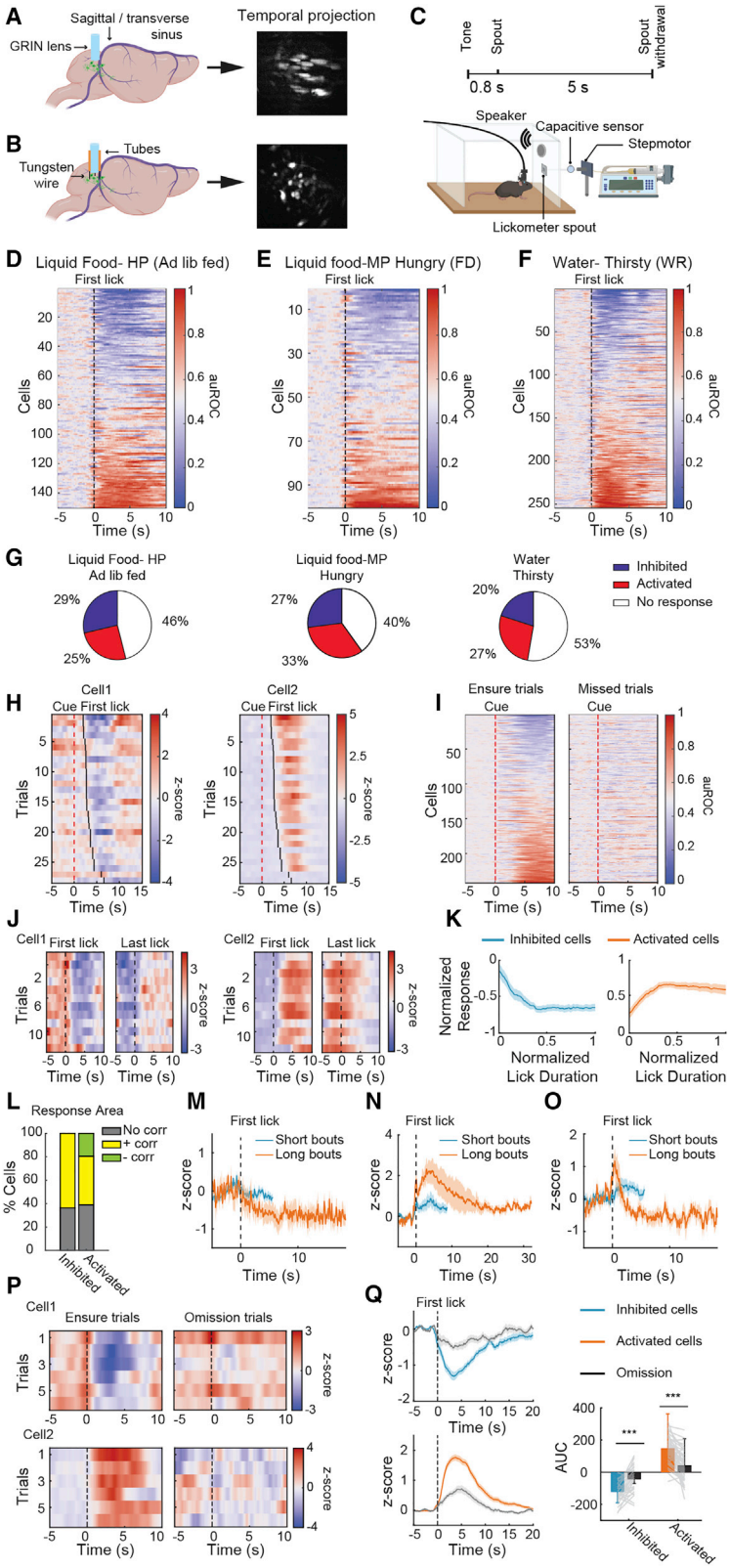

Figure 3. PeriLC^{VGLUT2} Neurons Respond during the Consummatory Phase of Hunger and Thirst

(A and B) GRIN lens schematic in the absence (left; A) and presence (left; B) of anchoring wires as well as the corresponding blurred field of view (FOV) (right; A) and stabilized FOV (right; B) from freely moving mice (1,000 frames).

(C) Schematic and experimental setup for cue-conditioned, lick-triggered consumption task.

(D–F) Ensemble response of periLC^{VGLUT2} neurons to high-palatability (HP) liquid food ingestion (Ensure) in *ad-libitum*-fed mice (D; n = 150 neurons, 2 mice), moderate palatability (MP) liquid food under FD (E; n = 100 neurons, 2 mice), and water under WR (F; n = 254 neurons, 3 mice). Black line: first lick.

(G) Proportion of neurons that show statistically significant activation or inhibition responses during ingestion in (D), (E), and (F).

(H) Two example periLC^{VGLUT2} neurons that were inhibited (left) or activated (right) upon the first lick of Ensure but were not modulated by the paired auditory cue across multiple trials. Red dashed line: auditory cue; black line: first lick.

(I) Ensemble response of periLC^{VGLUT2} neurons averaged across multiple trials (area under the receiver operating characteristic [auROC]) aligned with auditory cue in Ensure consummatory trials (left) and missed trials (right) in which mice received cue and spout but did not lick (n = 242 neurons, 3 mice).

(J) Two example periLC^{VGLUT2} neurons that were inhibited (left) or activated (right) aligned to the first lick of Ensure (left) and the last lick (right) across trials with different experimenter-controlled consumption times.

(K) Mean normalized response of significantly inhibited neurons (left, n = 25 neurons) or activated neurons (right, n = 37 neurons) during different experimenter-controlled consumption time windows.

(L) Proportion of neurons from the inhibited and activated subpopulations (see STAR Methods) whose integrated responses show statistically significant positive, negative, or no correlation with bout duration during self-paced Ensure consumption (n = 137 neurons, 3 mice).

(M–O) Example neurons from the inhibited (M) or activated (N and O) subpopulations where integrated response is positively correlated (M and N) or negatively correlated (O) with bout duration. Traces end with the last lick.

(P) Example periLC^{VGLUT2} neurons inhibited (top) or activated (bottom) in Ensure consummatory trials (left) and diminished responses in omission trials (right).

(Q) Responses of all inhibited neurons (top left, n = 35 neurons, 2 mice) and activated neurons (bottom left, n = 59 neurons, 2 mice) as well as corresponding AUC for these two subpopulations in consummatory and omission trials (right). Shaded area: ±SEM. Error bars: SD. ***p < 0.001. Statistics: Table S1.

subpopulation, track consumption duration in self-paced feeding bouts.

We investigated the possibility that periLC^{VGLUT2} neuron activity is related to motor control of consumption in FD-mice by intermingling consumption trials with omission trials, in which mice still licked the spout but did not receive food. Omission trials showed greatly diminished periLC^{VGLUT2} neuron modulation (Figures 3P, 3Q, and S3P). We also measured the responses of both activated and inhibited subpopulations of periLC^{VGLUT2} neurons in experimenter-controlled consumption, in which the lick spout delivered food for different access times (5–12 s) in hungry mice (Figures S3Q and S3R). Only a few inhibited neuron responses during the consumption window were significantly correlated with lick number (2%) or lick frequency (<1%) (Figure S3S), further ruling out a substantial role of periLC^{VGLUT2} neurons in direct motor-control of consumption. Instead, these experiments consistently showed that the activity of periLC^{VGLUT2} neurons is tied to food or water ingestion.

Hunger and Thirst Influence periLC^{VGLUT2} Neurons

Our experiments showed that activation or inhibition of periLC^{VGLUT2} neurons decreased or increased food intake, respectively, and *in vivo* calcium imaging revealed that periLC^{VGLUT2} neurons are subdivided into subpopulations that are selectively activated or inhibited during the consumption bout. This might include multiple potential causal relationships between the measured activity patterns of these functionally defined subpopulations of periLC^{VGLUT2} neurons and consumption bouts. One possibility was that these two subpopulations of periLC^{VGLUT2} neurons oppositely regulated consumption bouts (models 1 and 2, Figures 4A and 4B). Alternatively, both subpopulations of periLC^{VGLUT2} neurons might regulate consumption bouts similarly, despite being oppositely regulated by consumption (models 3 and 4, Figures 4C and 4D). Model 4 (Figure 4D) could be excluded because activation of the entire periLC^{VGLUT2} neuron population would be predicted to increase consumption, which is opposite to what we observed experimentally (Figure 2H). To consider the remaining possibilities, we performed additional *in vivo* calcium imaging experiments to characterize how these periLC^{VGLUT2} neuron subpopulations were modulated by progressive consumption and hunger or thirst.

Model 1 (Figure 4A) is a negative feedback model, which would limit consumption and suppress further ingestion. For a negative feedback model, we anticipated that the activated and inhibited periLC^{VGLUT2} neuron subpopulations would show consumption bout-driven responses that would become progressively larger with food intake in conjunction with the reduction in feeding bout size that is observed from hunger to satiety (Figure S3L; Davis and Perez, 1993). First, we investigated whether the neuronal dynamics of either subpopulation showed increased response amplitude with successive trials of food or water intake. For FD or WD mice, neither the mean response amplitude nor baseline calcium activity of all periLC^{VGLUT2} neurons or the inhibited or activated subpopulations were significantly correlated with trial number (Figures 4E–4J and S4A–S4F), although the amount consumed during the sessions was insufficient to lead to satiety. For a small proportion of individual periLC^{VGLUT2} neurons in FD or WD mice, there was a significant correlation with the consumption response amplitude across trials but not for the baseline activity. However, most of these significantly correlated neurons showed gradually reduced activation or inhibition responses with successive trials (Figures S4G–S4J). The unchanged or reduced magnitude of periLC^{VGLUT2} neuron responses with increased food or water intake is not consistent with progressive integration of consumption bouts to suppress eating or drinking.

Next, we tested how energy-deficit or dehydration states would modulate periLC^{VGLUT2} neuron responses. When ensemble neural responses to Ensure consumption were compared between an *ad-libitum*-fed state and FD state on separate days, the amplitude of both the activated and the inhibited responses was significantly larger in FD mice (Figures S4K and S4L). To reliably match imaged neurons between hunger or thirst and satiety, we also examined the response of periLC^{VGLUT2} neurons after refeeding or rehydrating from FD or WD to satiety in experiments in which small-volume (3 μL) consumption trials were interspersed with longer free-access periods (Ensure consumption: 3–4 mL, water consumption: 0.4–0.6 mL) to achieve satiation (assessed by increased "misses" in cue-conditioned consumption trials). For hunger and thirst, we found that both activated and inhibited responses from FD mice and WD mice were reduced in the same neurons after satiation with food (Figures 4K–4M) or water (Figures 4N–4P). Similar proportions of significantly activated and inhibited neurons were observed during Ensure consumption in hunger and satiety, despite the difference in magnitude for their responses (Figure S4M). For WD mice, satiety reduced the proportion of significantly activated and inhibited neurons (Figure S4M). These experiments demonstrate that periLC^{VGLUT2} neuron response magnitudes are larger in hunger and thirst states than in satiety states.

Based on the modulation of periLC^{VGLUT2} neuron dynamics by hunger or thirst relative to satiety, we could further constrain models of how periLC^{VGLUT2} neuron activity is causally related to food consumption. Because responses of activated and inhibited periLC^{VGLUT2} neuron subpopulations are largest in hunger and thirst states, the causal relationships in model 1 (Figure 4A) and the left side of model 3 (Figure 4C) predict either reduced drive or stronger inhibition of consumption bouts in hunger or thirst relative to satiety, but this is opposite to observations that consumption bout duration is longest in hunger and thirst states (Figure S3L; Cabanac, 1985; Davis and Perez, 1993; Spector et al., 1998). In addition, the left side of model 2, where the consumption-activated subpopulation (Figure 4B, left side) promotes consumption, is also not consistent with optogenetic and chemogenetic perturbation data (Figure 2). This leaves the right side of model 2 and 3, in which the inhibited subpopulation shows a double-negative feedback causal relationship (functionally similar to positive feedback) between neuron activity and behavior. The inhibited subpopulation of model 2 and 3 is consistent with the observed data that (1) activation inhibits consumption and inhibition promotes consumption, (2) hunger and thirst increase the amplitude of the inhibited subpopulation's response, (3) longer consumption bouts are associated with sustained inhibition in a majority of the inhibited periLC^{VGLUT2} neuron subpopulation, and (4) some activated neurons become inhibited with longer consumption bouts (Figures 3L–3O). These

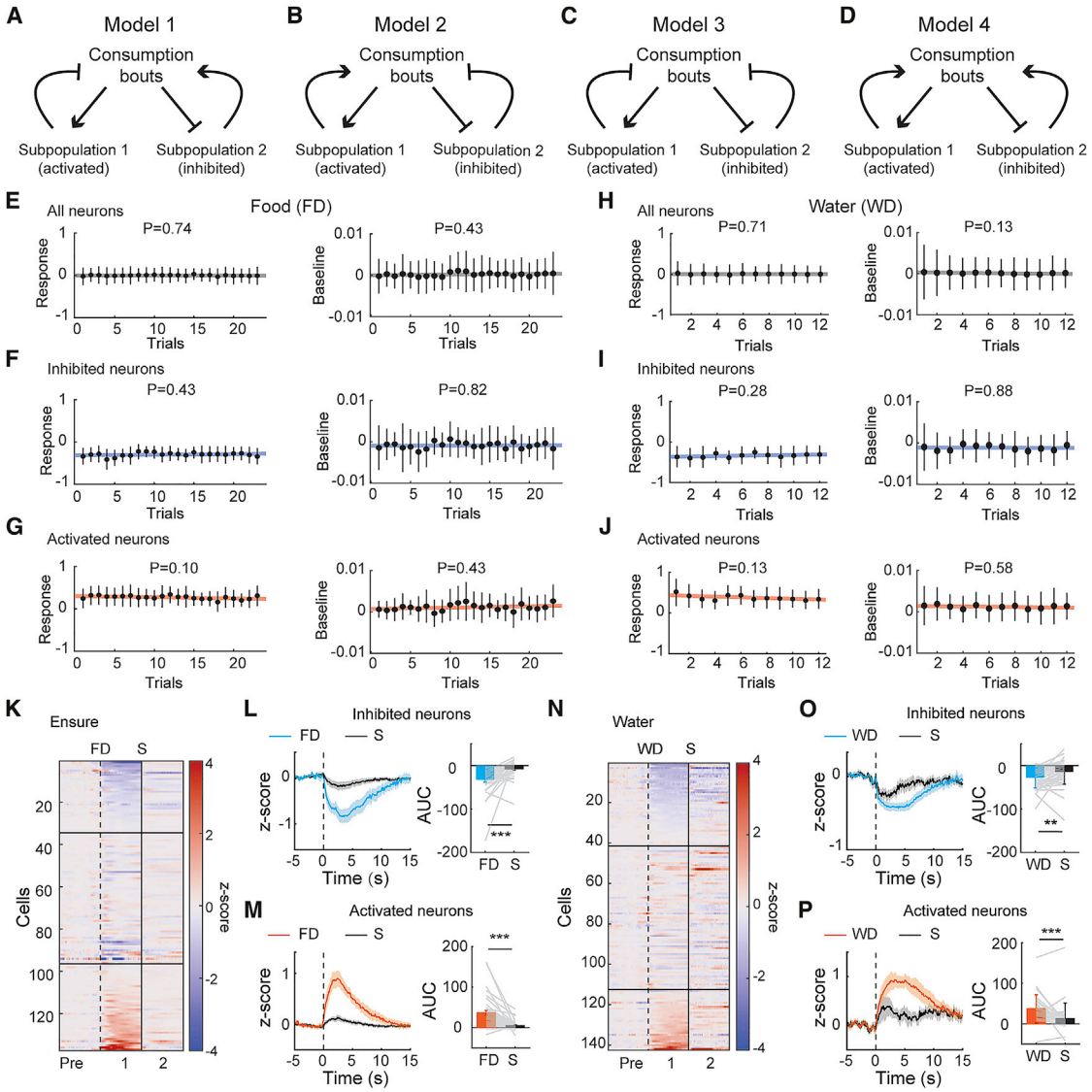

Figure 4. Hunger and Thirst Modulate Response Magnitude of periLC^{VGLUT2} Neurons

(A–D) Hypothetical models for causal relationships of the effects of periLC^{VGLUT2} neuron activity on consumption bouts. Arrows: activate. Bars: inhibit.

(E–G) Mean normalized response amplitude (left) and mean baseline (right) of all the neurons (E), the inhibited (F), and the activated (G) subpopulations across successive liquid food consumption trials in FD mice (before satiety). Thick line: linear regression fit.

(H–J) The same as (E), (F), and (G) for water consumption with WD mice.

(K) Ensemble response of periLC^{VGLUT2} neurons to Ensure consumption (3 μL) in FD mice and after reaching satiety (S) following multiple self-paced consumption trials (n = 137 neurons, 3 mice).

(L and M) Responses (left) of all the significantly inhibited (L; n = 34, 3 mice) or activated (M; n = 43, 3 mice) neurons as well as their cell-matched AUC (right) under FD or satiety state. Dashed line: first lick.

(N) The same as K for water consumption in WD mice (n = 142, 3 mice).

(O and P) The same as (L) and (M) for water consumption (inhibited neurons: n = 41; activated neuron: n = 30; 3 mice). Dashed line: first lick. Solid vertical line: boundary of trials during FD or WD and satiety. Solid horizontal lines: division of significantly inhibited (top) or activated (bottom) subpopulations. Shaded area: ± SEM. Error bars: SD. **p < 0.01, ***p < 0.001. Statistics: Table S1.

data do not rule out a contributing role for the activated subpopulation, but our analysis of the neuronal dynamics and perturbation experiments indicates a dominant effect of the inhibited subpopulation for explaining the causal relationships between neuron dynamics and functional perturbation experiments on eating and drinking.

Consumption-Inhibited periLC^{VGLUT2} Neurons Are Scaled by Palatability

Because periLC^{VGLUT2}-neuron-inhibition-promoted food intake, was rewarding, and neural responses were largest during hunger and thirst, we hypothesized that this subpopulation may be related to food palatability. To examine this, we first measured

periLC^{VGLUT2} neuron responses in FD mice to 4-fold-diluted Ensure, which was less avidly consumed than full-strength Ensure by *ad-libitum*-fed and hydrated mice, indicating reduced palatability (licks within 1 h, Ensure: 1,630 ± 372 licks, diluted Ensure: 813 ± 203 licks). Correspondingly, the response magnitude of periLC^{VGLUT2} neurons in FD mice is significantly reduced for diluted Ensure even when the same quantity was consumed (Figures 5A–5C). Thus, periLC^{VGLUT2} neuron responses are scaled by food palatability.

Next, we monitored periLC^{VGLUT2} neuron activity during the consumption of tastants with different palatability. We used cue-conditioned small-volume (3 μL) consumption trials in which the entire tastant solution was consumed for each trial by WR mice, regardless of palatability. The tastants included sucrose (300 mM), quinine (1 mM), citric acid (50 mM), low salt (60 mM), and high salt (500 mM), and each of these tastants elicited activated and inhibited responses of periLC^{VGLUT2} neurons (Figure S5A). Unsupervised k-means clustering of responses to both Ensure and water consumption within the same sessions demonstrated that inhibited or activated neurons were from the same subgroup for each reward (Figure 5D). We compared the responses from consumption of palatable Ensure and sucrose solutions and found similar responses (Figure 5E). In separate experiments, unpalatable solutions with either citric acid and high salt (Figure 5H) or quinine and citric acid (Figure 5I) also activated and inhibited similar subgroups of periLC^{VGLUT2} neurons. However, when neuron responses to palatable Ensure or sucrose were compared to the consumption of bitter quinine, separate sets of periLC^{VGLUT2} neurons were activated (Figures 5F and 5G). Thus, for tastants with opposite valence, such as Ensure and quinine or sucrose and quinine, the activated periLC^{VGLUT2} neurons segregated by taste valence, although a greater proportion of the activated neurons was associated with palatable tastants. For tastants with the same valence, ensemble response patterns were similar (Figures 5D, 5E, 5H, and 5I). We found one exception to this with a comparison of low salt and high salt, which have opposite valence but showed similar responses (Figures S5C and S5D), possibly related to a role of some neurons from this region in salt balance (Geerling and Loewy, 2006; Lee et al., 2019; Shin et al., 2011).

The inhibited population of periLC^{VGLUT2} neurons formed a large proportion of the modulated neurons across multiple tastants. Moreover, the same periLC^{VGLUT2} neurons were inhibited across different tastants, such that the inhibited neurons did not segregate by taste valence in WR mice (Figures 5D–5I). Even opposite valence tastants, such as Ensure and quinine or sucrose and quinine, showed the same group of inhibited periLC^{VGLUT2} neurons during consumption (Figures 5F and 5G), all of which offer a high water content that is valued in the thirst state. Nevertheless, when the response magnitudes of the inhibited clusters were compared across these oppositely valenced tastants within a session, we found that the more palatable tastants showed a greater inhibition of periLC^{VGLUT2} neurons. The inhibitory response magnitude to Ensure was significantly larger than that for water or quinine (Figures 5J and 5L). Moreover, the quinine-inhibited response was also significantly smaller than that for sucrose or citric acid (Figures 5M and 5O). There was no significant difference in the responses of the inhibited periLC^{VGLUT2} neurons to tastants with similar valence, such as between Ensure and sucrose or between citric acid and high salt (Figures 5K and 5N). Palatability-scaled responses across different tastants were not observed with the activated periLC^{VGLUT2} neurons for tastants with similar valence (Figure S5B). Thus, *in vivo* calcium imaging revealed that activated periLC^{VGLUT2} neurons encode taste valence information, whereas inhibited periLC^{VGLUT2} neurons were broadly tuned across different tastants and had response amplitudes scalable to the palatability of the consumed solution.

Together, consumption bout lengthening associated with suppression of the inhibited neurons in models 2 and 3 (Figures 4B and 4C, right side) was consistent with the enhanced inhibitory response to food deprivation (Figures 4K–4M) and to palatable tastes (Figures 5J–5O). Although there is a possibility that reduced food intake from periLC^{VGLUT2} neuron activation was due to the negative taste valence neurons (model 2-alt, Figure S5E), the suppression of these bitter-activated neurons in Figure S5E is not expected to be responsible for increased consumption of sweet, palatable (non-bitter) food (Figure 2D). Moreover, suppression of periLC^{VGLUT2} neuron function with tetanus toxin expression did not affect quinine avoidance, indicating that periLC^{VGLUT2} neurons (Figure S5F) are not necessary for suppressing the ingestion of bitter tastants.

Temporally Precise Modulation of Ingestion

Our model (model 2, right side; Figure 4B) shows a double-negative feedback relationship that predicts periLC^{VGLUT2} neuron inhibition during consumption will potentiate subsequent food consumption similarly to the effects of increased palatability either by hunger or thirst state or by the hedonic value of the consumed items. Chemogenetic inhibition of periLC^{VGLUT2} neurons increased eating (Figures 2A–2D) but does not mimic the consumption-locked neuronal dynamics that we measured *in vivo*. In light of this finding, we tested whether optogenetic inhibition of periLC^{VGLUT2} neurons solely during food and water consumption would have behavioral consequences associated with increased palatability. Our hypothesis was that inhibition of periLC^{VGLUT2} neurons selectively during ingestion was critical for increasing consumption. To assess the importance of inhibition during consumption (closed loop), we also investigated whether randomly delivered periLC^{VGLUT2} neuron photoinhibition (open loop) would influence consumption.

We expressed ArchT in periLC^{VGLUT2} neurons and designed a closed-loop optical inhibition experiment in which photoinhibition was contingent on food consumption and sustained only during ingestion (Figure 6A). To avoid a ceiling effect, we used diluted Ensure so that it was only modestly consumed by *ad-libitum*-fed mice. To assess the temporal properties of the lick-triggered periLC^{VGLUT2} neuron inhibition on self-initiated food intake, we used interleaved blocks (2 min) alternating between lick-contingent photoinhibition blocks and no-laser blocks. For the same animals, we also tested open-loop conditions with noncontingent photoinhibition, in which the number and duration of laser pulses were yoked to the contingent photoinhibition experiments but delivered independently of whether the mouse was licking. In addition, we performed a sham session with no photoinhibition in any of the blocks (Figure 6B). These different

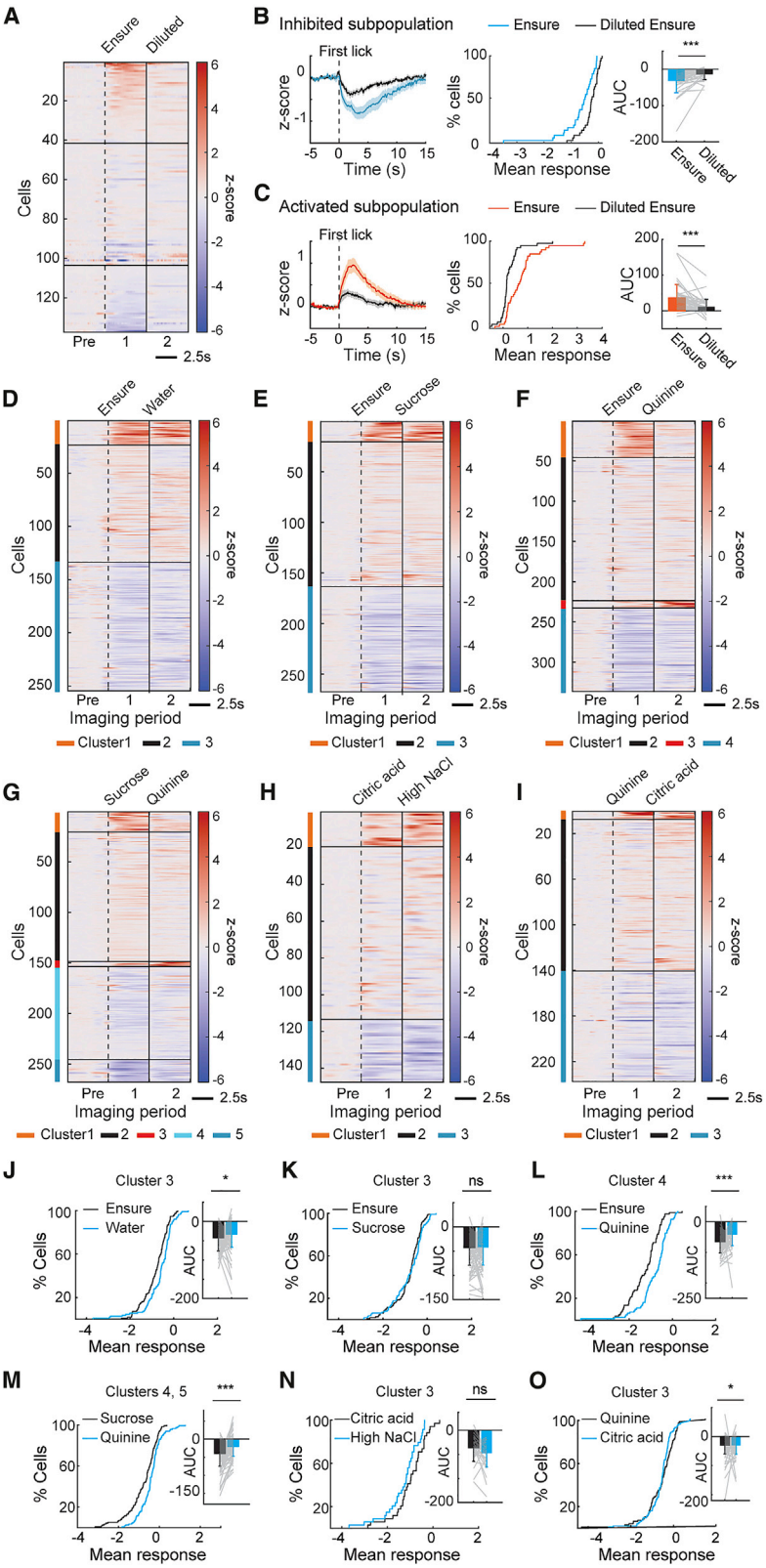

Figure 5. Consumption-Inhibited periLC^{VGLUT2} Neuron Response Tracks Palatability

(A) Ensemble response of periLC^{VGLUT2} neurons to Ensure or less palatable, diluted Ensure consumption under FD (n = 137 neurons, 3 mice). Solid horizontal lines: significantly inhibited (top) or activated (bottom) subpopulations. Dashed vertical line: first lick. Solid vertical line: boundary between Ensure and diluted Ensure consumption.

(B) Responses of all significantly inhibited neurons to Ensure (left, shaded area: ± SEM), their mean response distribution (middle), and corresponding cell-matched AUC (right) (n = 41 neurons, 3 mice).

(C) The same as (B) but for all the significantly activated neurons (n = 34, 3 mice).

(D–I) Response of periLC^{VGLUT2} neurons to Ensure and water (D; n = 254 neurons, 3 mice), Ensure and sucrose (E; n = 267 neurons, 3 mice), Ensure and quinine (F; n = 336 neurons, 4 mice), sucrose and quinine (G; n = 267 neurons, 3 mice), citric acid and high salt (H; n = 147 neurons, 2 mice), and quinine and citric acid (I; n = 237 neurons, 3 mice) grouped by k-means clustering. Solid horizontal line: boundary for each k-means cluster. Dashed vertical line: first lick. Solid vertical line: boundary between two tastants.

(J–O) Cumulative distribution of the mean response and the corresponding cell-matched AUC comparison for the broadly tuned inhibited neurons shown in cluster 3 of (D) (J), cluster 3 of (E) (K), cluster 4 of (F) (L), clusters 4 and 5 of (G) (M), cluster 3 of (H) (N), and cluster 3 of (I) (O). E, Ensure; W, water; S, sucrose; Q, quinine; C, citric acid; HN, high salt. ns, $p > 0.05$; *$p < 0.05$; ***$p < 0.001$. Error bars: SD. Statistics: Table S1.

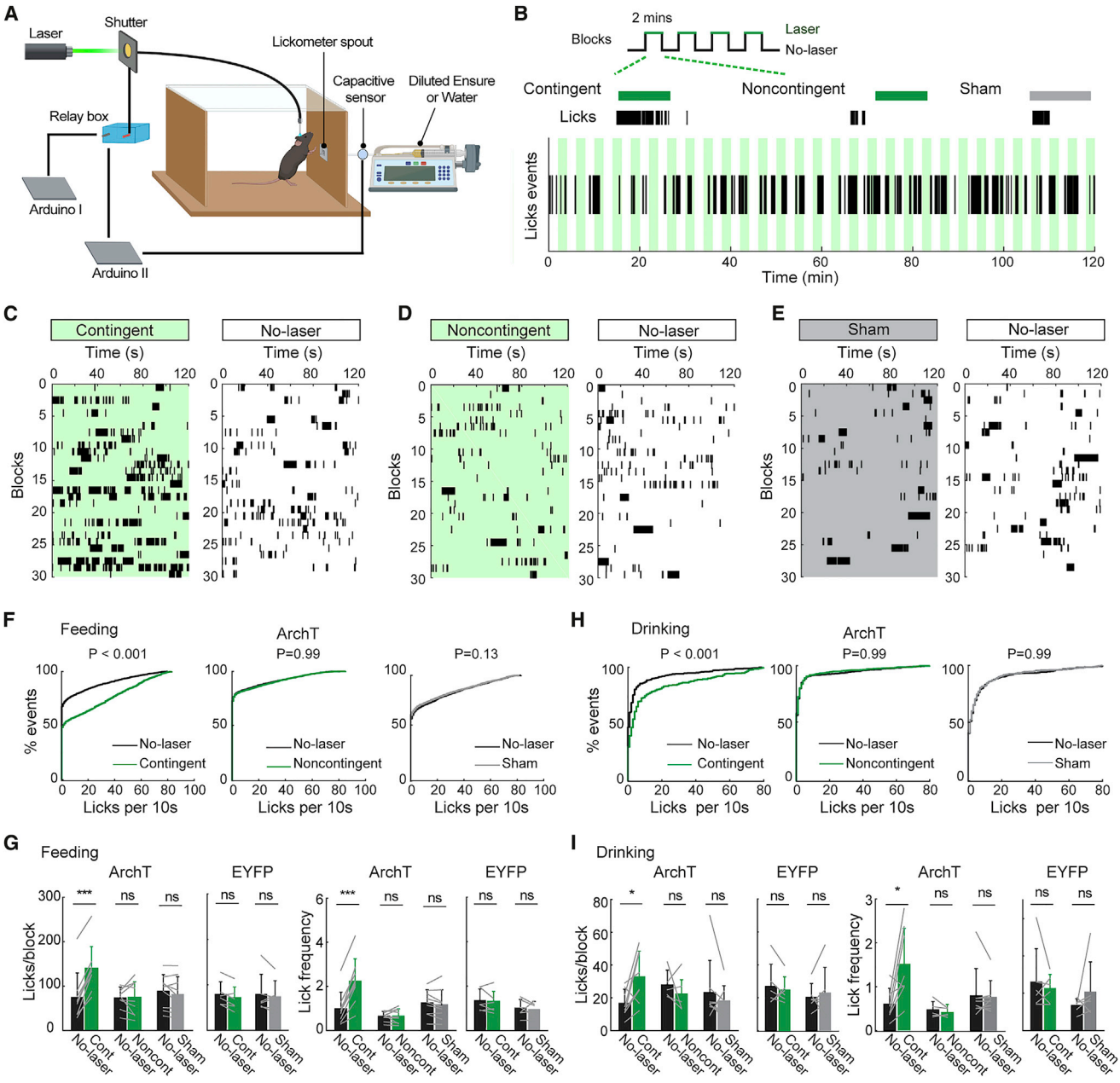

Figure 6. Lick-Contingent Inhibition of periLC^{VGLUT2} Neurons Increases Feeding and Drinking

(A) Schematic of experimental setup for lick-triggered photoinhibition.

(B) Schematic of interleaved trial structure for the contingent, noncontingent, and sham perturbation paradigms and example of lick events (black tick marks) in one session. Trials (2 min) alternated between laser-on blocks (green) and control no-laser blocks (white). The laser-on blocks were either lick triggered (contingent), lick independent (noncontingent), or sham (no laser in any of the trials).

(C–E) Examples of lick events for diluted Ensure in contingent (C), noncontingent (D), and sham (E) sessions for laser-on (left) and laser-off (right) blocks from the same mouse. Black tick: lick.

(F) Cumulative distribution of the lick events analyzed in 10-s bins in the contingent (n = 9), noncontingent (n = 9), and sham conditions (n = 9) from laser-on and laser-off blocks during diluted Ensure consumption.

(G) Mean lick number (left) and lick frequency (right) of the blocks that contain lick events in both laser-on and -off blocks during the contingent (cont), noncontingent (noncont), and sham paradigms in ArchT mice and EYFP mice.

(H and I) As in (F) and (G) for water consumption in WR mice. ns, $p > 0.05$; *$p < 0.05$; ***$p < 0.001$. Error bar: SD. Statistics: Table S1.

experimental paradigms were designed to examine the short-term effects of periLC^{VGLUT2} neuron modulation on the magnitude of consumption.

For blocks with lick-contingent photoinhibition of periLC^{VGLUT2} neurons, mice consumed more food than for blocks lacking photoinhibition (Figure 6C). In contrast, for noncontingent photoinhibition or no-laser sessions, mice did not consume more between the two alternating blocks (Figures 6D and 6E). The cumulative distribution of lick events in contingent perturbation blocks was significantly greater than the interleaved no-laser blocks of the same session for ArchT mice but not EYFP controls (Figures 6F and S6A). Mean lick number per block, lick frequency, and total licks were also significantly increased only during contingent photoinhibition, and there was no significant difference for the two sets of consumption blocks for either noncontingent or the sham perturbation sessions in ArchT mice or in EYFP controls (Figure 6G and S6B). In contrast, mice with injections that mistargeted expression of ArchT in VGLUT2 neurons of the caudal PCG showed the opposite effect, where they reduced food intake under both contingent and noncontingent conditions and also induced conditioned place avoidance (Figure S6C), and mistargeting to the cerebral ventricle or LDT showed no significant effects during photoinhibition (Figure S6D). These results demonstrate that the effects on consumption were specific to inhibition in the anterior periLC.

We also examined whether consumption changed across trials during the session, but there was no significant difference in consumption in the first half versus the second half of the session under all the conditions (Figure S6E). Thus, we did not see evidence of within-session learning to consume more food after repeated pairing with interleaved periLC^{VGLUT2} neuron inhibition.

Next, we also determined the effect of photoinhibition on water consumption by using mildly dehydrated mice (see STAR Methods). ArchT mice, but not EYFP mice, in the contingent photoinhibition blocks (1 min) increased water consumption (Figures 6H and 6I). Notably, this finding was different than our results obtained using chemogenetic inhibition, which failed to significantly increase water intake (Figure S2D). There was not a significant difference between blocks for either noncontingent photoinhibition or sham conditions (Figures 6H, 6I, and S6F–S6J). These experiments show that periLC^{VGLUT2} neuron inhibition increased both food and water intake only when inhibition was paired with consumption, which mimics the natural dynamics of periLC^{VGLUT2} neurons.

Selective Control of Consumption Duration but Not Initiation

Consumption initiation and maintenance are mediated by separate processes (Figure 1A; Berridge, 1996; Taha et al., 2009; Wassum et al., 2009). Attraction to a previously reinforced location is a process related to approaching the location of food or water when hungry or thirsty and is sometimes associated with "wanting" (Berridge, 1996; Wassum et al., 2009). However, periLC^{VGLUT2} neuron dynamics were consistent with a role in controlling palatability, which is a complementary aspect of motivation associated with increased "liking," and leads to prolongation of consumption once it is initiated (Berridge, 1996; Wassum et al., 2009). To distinguish these behavioral mechanisms of periLC^{VGLUT2} neuron photoinhibition on consumption, we examined the relationship between the initiation and the duration of consumption by analyzing the microstructure of licking events in contingent and noncontingent photoinhibition experiments. This approach has been used previously to deconstruct different aspects of feeding behavior control (Davis, 1973; Davis and Smith, 1992; Johnson et al., 2010; Spector et al., 1998).

We first determined whether periLC^{VGLUT2} neurons altered the fundamental lick frequency, which is controlled by hindbrain central pattern generators (Wiesenfeld et al., 1977). The fundamental lick frequency was derived from the first peak (mu1) and the second peak (mu2) of the inter-lick-interval (ILI) histogram and showed no difference between perturbation blocks and no-laser blocks for either contingent or noncontingent inhibition with either Ensure or water consumption (Figure S7A). This finding is consistent with expectations from our imaging results, which showed that periLC^{VGLUT2} neurons were not directly related to the motor control of licking (Figures 3P, 3Q, and S3Q–S3S).

Next, we determined the effect of periLC^{VGLUT2} neuron photoinhibition on the number and duration of feeding bouts. A feeding bout was defined by an ILI threshold that was derived from the animal's time within the food zone (FZ) during consumption (Figures S7B and S7C; see STAR Methods). The duration of feeding bouts was significantly increased for photoinhibition of periLC^{VGLUT2} neurons that was contingent on consumption but was not significantly increased for noncontingent inhibition or sham conditions (Figure 7A) or for EYFP control mice (Figure S7D). Similarly, water consumption bouts were prolonged only with contingent photoinhibition (Figures 7D and S7E).

We found that the cumulative distribution of bout duration for both feeding and drinking was best fit by an exponential distribution (see STAR Methods), indicating that maintaining a consumption state could be described by a Markov process with a fixed transition probability per unit time. The time constant of this exponential was approximately twice as long for contingent photoinhibition than the no-laser blocks (Figures 7B and 7E; Table S2). The inverse of this time constant is the probability of leaving (P_{leave}) the consummatory state. The probability of staying in the consummatory state ($P_{stay} = 1 - P_{leave}$) was increased in ArchT mice due to periLC^{VGLUT2} neuron inhibition from 91.6% → 95.5% per second (food) and 88.7% → 92.4% per second (water) but not in EYFP mice (see Table S2). These probability shifts were associated with a large cumulative effect on consummatory bout duration (Figure S7F) and were statistically significant ($p < 0.001$) (Figures S7G).

The number of consumption bouts represents state transitions from the satiety to the preparatory phase of motivated behavior that brings the animal to the source of food or water. In contrast to the lengthening of feeding and drinking bout duration, the number of bouts was either unchanged (food) or decreased (water) by contingent, noncontingent, and sham photoinhibition of periLC^{VGLUT2} neurons (Figures 7C and 7F). Moreover, the noncontingent photoinhibition trials further ruled out an alternative role of the inhibited periLC^{VGLUT2} neuron subpopulation in controlling the transition from satiety → preparatory phase. This would be predicted to increase the number of food ingestion

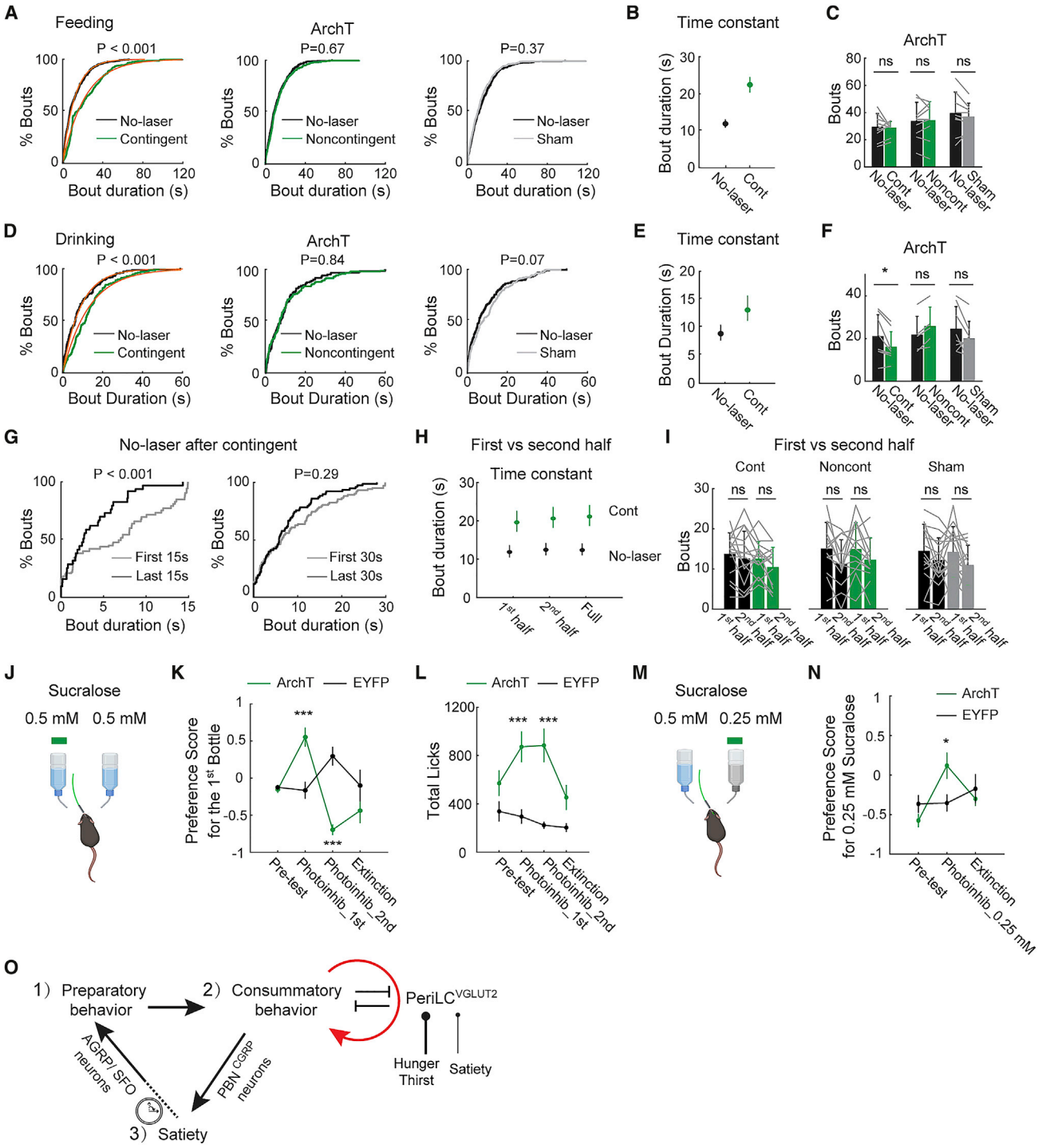

Figure 7. PeriLC^{VGLUT2} Inhibition Sustains Consumption Duration and Shifts Palatability

(A) Cumulative distribution of lick bout duration in contingent, noncontingent, and sham conditions from laser-on and -off blocks in periLC^{VGLUT2} ArchT mice during diluted Ensure consumption. Orange line: exponential curve fit for the distribution of feeding bouts duration.

(B) Time constant from exponential curve fitting of the cumulative distribution of lick bout duration in the contingent condition. Error bar: 95% confidence interval.

(C) Number of bouts of Ensure consumption in different conditions from periLC^{VGLUT2} ArchT mice.

(D–F) As in (A)–(C) for water consumption in WR mice.

(G) Cumulative distribution of bout duration from the initial 15 s and the last 15 s (left) or the initial 30 s and the last 30 s (right) in the no-laser blocks following contingent blocks that contain feeding bouts straddling the next no-laser block in periLC^{VGLUT2} ArchT mice.

(legend continued on next page)

bouts in noncontingent photoinhibition experiments relative to the no-laser blocks, which was not observed.

When a shorter bout threshold (1 s) was used for both feeding and drinking, we also found a significant increase in bout duration for ArchT mice only during contingent photoinhibition, without a corresponding increase in bout number (Figures S7H–S7M).

Next, we examined the timescale after cessation of photoinhibition that would continue to influence consumption by analyzing feeding bouts that straddled the contingent photostimulation and no-laser blocks. Consummatory bout duration was significantly longer in the first 15 s of the no-laser blocks following termination of lick-triggered photoinhibition blocks than in the last 15 s of the same blocks (Figure 7G), which was not observed for noncontingent or sham paradigms (Figure S7N). This difference was not statistically significant with a longer time window (30 s). Thus, the effect of periLC^{VGLUT2} neuron inhibition on consumption extinguishes 15–30 s after cessation of photoinhibition. Consistent with this finding, we did not find a significant difference for the lick-contingent paradigm for which we analyzed consumption duration or initiation of consumption bouts from the first and second half of the sessions (Figures 7H and 7I) or from two consecutive sessions (Figures S7O and S7P). Thus, we did not detect long-term learning effects when alternating contingent and no-laser blocks, which limits the role of periLC^{VGLUT2} neurons to a short-term adaptive role associated with palatability during ingestion.

PeriLC^{VGLUT2} Neuron Modulation of Palatability

To further evaluate the causal relationship of periLC^{VGLUT2} neurons to palatability-guided consumption, we performed closed-loop optogenetic inhibition in mice expressing ArchT or EYFP during two bottle preference tests. In the first experiment, a nonnutritive sweetener solution (sucralose, 0.5 mM) was available simultaneously from two bottles (Figure 7J). Lick-triggered photoinhibition of periLC^{VGLUT2} neurons led to preferential consumption, which was reversible to the other bottle after switching the paired inhibition site in a subsequent session. There was no significant preference for either bottle in an extinction test with no photoinhibition in ArchT mice, nor in EYFP mice during lick-contingent laser stimulation (Figures 7K and 7L).

Next, we examined whether consumption preference could be shifted to a low sucralose concentration (0.25 mM) paired with lick-contingent periLC^{VGLUT2} neuron photoinhibition in the presence of a higher sucralose concentration (0.5 mM) (Figure 7M). A significant increase of preference index for the lower concentration sucralose was induced in ArchT but not EYFP mice, and this preference reversed to the higher sucralose concentration for ArchT mice in a photoinhibition extinction session (Figure 7N). Thus, lick-contingent photoinhibition of periLC^{VGLUT2} neurons reversibly upshifts consummatory preferences, further confirming the role for promoting palatability-guided consumption.

DISCUSSION

Here, we report that periLC^{VGLUT2} neurons selectively control the duration of the consummatory phase of ingestive behaviors by conveying palatability information. PeriLC^{VGLUT2} neuron inhibition response magnitude is scaled by palatability and homeostatic need state. Correspondingly, periLC^{VGLUT2} neuron inhibition increases food and water consumption and shifts taste preference. Inhibited periLC^{VGLUT2} neurons play a convergent role in hunger and thirst by increasing the probability of staying in a consumption state. This is analogous to the experience of ingesting tasty food or beverages that compels further consumption. These properties reveal a common substrate for hunger and thirst that controls consumption by altering palatability.

Our data indicate that periLC^{VGLUT2} neurons do not directly control the specific motor actions of consumption, for example periLC^{VGLUT2} neuron inhibition does not elicit fictive ingestive behaviors or alter the fundamental lick frequency. Instead, periLC^{VGLUT2} neurons have a modulatory role, primarily during the consummatory phase of behavior, for which inhibition increases the probability of maintaining consumption (Figure 7O), leading to longer consumption bouts. PeriLC^{VGLUT2} neuron response magnitude increases with hunger, thirst, and palatability, each of which lengthens consummatory bouts. In satiety, periLC^{VGLUT2} neurons show a reduced response magnitude, which reduces the probability of maintaining consumption. This complements PBN^{CGRP} neurons, in which the activity during nonconsummatory periods progressively increases and mediates the long-term satiety that accumulates over the course of a meal (Campos et al., 2016, 2018).

Palatability is a property that reflects the hedonic value of food, and it feeds back onto and promotes additional consummatory behavior. The complementary properties of consumption-inhibited periLC^{VGLUT2} neurons and the rewarding consequence of their inhibition to increase consumption are part of a double-negative feedback relationship, which is functionally analogous

(H) Time constant from exponential curve fitting for the lick bout duration distribution comparing no-laser blocks to corresponding contingent photoinhibition blocks in ArchT mice from the first-half, the second-half, or the full session during diluted Ensure consumption. Error bar: 95% confidence interval.
(I) Feeding bouts from the first-half and the second-half sessions in ArchT mice.
(J) Schematic of two-bottle preference test using identical sucralose solutions (0.5 mM) with lick-triggered photoinhibition on one side.
(K) Preference score of the 1st-bottle across four sessions involving (1) pre-test with no photoinhibition, (2 and 3) lick-triggered photoinhibition at the 1st (2) or 2nd (3) bottle, and (4) extinction with no photoinhibition (ArchT mice: n = 8; EYFP mice: n = 8).
(L) Total licks across four sessions from (K).
(M) Schematic of preference test between 0.25 mM and 0.5 mM sucralose solutions across three sessions involving (1) pre-test with no photoinhibition, (2) lick-triggered photoinhibition at the 0.25 mM sucralose bottle, and (3) extinction with no photoinhibition.
(N) Preference score of 0.25 mM sucralose solution across three sessions (ArchT mice: n = 8; EYFP mice: n = 8).
(O) Three phases of motivated behavior, including a role for periLC^{VGLUT2} neuron inhibition during consumption, which prolongs the consummatory phase through double-negative feedback that is increased by hunger or thirst states and reduced in satiety. Ns, $p > 0.05$; *$p < 0.05$. Error bars: SD. Statistics: Table S1.

to positive feedback. The double-negative feedback relationship between the inhibited subpopulation of periLC^{VGLUT2} neurons and consumption behavior can account for prolongation of food and water consumption. This mechanism is constrained by the fact that neuron firing rates cannot fall below zero. Therefore, although it has characteristics similar to positive feedback, it is self-limiting, which means that palatability is not able to "lock" an animal into a consummatory state. This is a neural algorithm for controlling consumption duration whereby palatable foods more strongly inhibit periLC^{VGLUT2} neurons and more reliably sustain bout duration, thus increasing intake. The cellular and circuit implementation of hunger- and thirst-scaled dynamic responses remain to be determined.

The effect of periLC^{VGLUT2} neuron inhibition on prolonging consumption is short lived (~15 s), which is likely important so that the palatability experienced for one food is not transferred to a subsequently ingested food. Notably, the neuronal dynamics of periLC^{VGLUT2} neurons do not indicate a role in terminating food ingestion (Figure S3K). The self-sustaining feedback cycle is terminated by environmental distractors (e.g., NAc^{D1R} neurons) (O'Connor et al., 2015) or respiration (McElvain et al., 2018), and eventually meal-satiety circuits (e.g., PBN^{CGRP} neurons) (Campos et al., 2016, 2018).

Double-negative feedback control over ingestion is related to hedonic overeating, sometimes called the "salted-nut phenomenon" (Hebb, 2002), for which ingestion is sustained by a palatable taste regardless of the energetic state. Nevertheless, hunger is also well established to shift palatability, which is called alliesthesia (Cabanac, 1971). This effect is also familiar from subjective experience, as famously mentioned in *Don Quixote*: "The best sauce in the world is hunger…" (de Cervantes, 1615/2015).

Here, we focused on the portion of the periLC surrounding and intermingled with the anterior portion of the LC in the dorsolateral PCG (see STAR Methods). This population of VGLUT2-expressing neurons includes some preLC^{PDYN} neurons, a subpopulation reported to promote salt seeking (Lee et al., 2019). In addition, activation of PVH^{PDYN} neuron projections to the periLC has been shown to reduce food intake, which provides one functionally identified route to this brain area modulation by energy homeostasis circuits, and inhibition of neurons in the LC and periLC region without regard to cell type increases food intake (Li et al., 2019). Our experiments spatially constrain the area that is associated with increased food and water ingestion because inhibition of VGLUT2 neurons around the caudal portion of the LC suppresses food intake. Notably, the distribution of preLC^{PDYN} neurons extends to these caudal portions of the LC (Allen Brain Atlas), indicating the potential for further subdivision in functional specializations within the areas surrounding the LC.

Conclusions

Palatable food and beverage ingestion are regulated differently from homeostatic needs (Saper et al., 2002), but they do not involve entirely separate circuits. High-palatability food and beverages lead to hedonic overconsumption, which is a major factor contributing to obesity. Our findings emphasize the importance of periLC^{VGLUT2} neurons for modulating palatability and enhancing both food and water consumption. Further investigation of periLC^{VGLUT2} neurons may offer new insights for controlling hedonic feeding and its relationship to overeating behaviors.

STAR★METHOD

Detailed methods are provided in the online version of this paper and include the following:

- KEY RESOURCES TABLE
- RESOURCE AVAILABILITY
  - Lead Contact
  - Materials Availability
  - Data and Code Availability
- EXPERIMENTAL MODEL AND SUBJECT DETAILS
  - Mice
- METHOD DETAILS
  - Anatomical definition
  - Virus
  - Surgeries
  - HSV injections
  - GRIN lens implantation
  - Photostimulation *in vivo*
  - Fos-mapping
  - Histology and Imaging
  - Single neuron reconstruction visualization
  - Calcium imaging in freely moving mice
  - Food, false food, social interactions, ghrelin injection
  - Cue-conditioned consumption
  - Self-paced consumption
  - Taste coding by periLC^{VGLUT2} neurons
  - Neuron perturbations during behavior
  - Chemogenetic or optogenetic modulation of food or water intake
  - Conditioned Place Preference
  - Nose poke experiment
  - Quinine and Ensure consumption
  - Closed-loop food intake and water intake experiment
  - Two bottle preference test
- QUANTIFICATION AND STATISTICAL ANALYSIS
  - 2D registration and cell counting
  - Calcium Imaging Analysis
  - Analysis of closed-loop perturbation behavioral experiments
  - Statistics

SUPPLEMENTAL INFORMATION

Supplemental Information can be found online at https://doi.org/10.1016/j.cell.2020.07.031.

ACKNOWLEDGMENTS

Research was funded by Howard Hughes Medical Institute (S.M.S.). We thank D. Anderson and L.-C. Lo for Cre-dependent HSV; E. Boyden for ArchT virus; P. Zhou for data processing advice; J. Winnubst and J. Chandrashekar for visualization of single neuron reconstruction; A. Hu and M. Copeland for histology; L. Ryan, C. Lopez, and M. Rose for behavior support; and L. Ryan and S. Lindo for viral injections. D. Stern, M. Ahrens, and Y. Lu commented on the manuscript.

AUTHOR CONTRIBUTIONS

Conceptualization, R.G. and S.M.S.; Experiment design, R.G. and S.M.S.; Data collection, R.G.; Data analysis for Fos and HSV brain mapping, R.G., Y.Y., and S.X.; Calcium imaging setup, R.G. and S.X.; Calcium imaging data analysis, R.G. and S.X.; Behavior control system, R.G. and S.X.; Behavior data analysis, R.G. and A.H. The manuscript was written by R.G. and S.M.S. with input from all authors.

DECLARATION OF INTERESTS

S.M.S. has served on the Scientific Advisory Board of Inscopix, Inc. and owns stock in the company.

Received: November 1, 2019
Revised: May 12, 2020
Accepted: July 21, 2020
Published: August 24, 2020

REFERENCES

Allen, W.E., Chen, M.Z., Pichamoorthy, N., Tien, R.H., Pachitariu, M., Luo, L., and Deisseroth, K. (2019). Thirst regulates motivated behavior through modulation of brainwide neural population dynamics. Science *364*, 253.

Aponte, Y., Atasoy, D., and Sternson, S.M. (2011). AGRP neurons are sufficient to orchestrate feeding behavior rapidly and without training. Nat. Neurosci. *14*, 351–355.

Atasoy, D., Betley, J.N., Su, H.H., and Sternson, S.M. (2012). Deconstruction of a neural circuit for hunger. Nature *488*, 172–177.

Avants, B.B., Tustison, N.J., Song, G., Cook, P.A., Klein, A., and Gee, J.C. (2011). A reproducible evaluation of ANTs similarity metric performance in brain image registration. Neuroimage *54*, 2033–2044.

Berridge, K.C. (1996). Food reward: brain substrates of wanting and liking. Neurosci. Biobehav. Rev. *20*, 1–25.

Betley, J.N., Cao, Z.F., Ritola, K.D., and Sternson, S.M. (2013). Parallel, redundant circuit organization for homeostatic control of feeding behavior. Cell *155*, 1337–1350.

Betley, J.N., Xu, S., Cao, Z.F.H., Gong, R., Magnus, C.J., Yu, Y., and Sternson, S.M. (2015). Neurons for hunger and thirst transmit a negative-valence teaching signal. Nature *521*, 180–185.

Bogovic, J.A., Hanslovsky, P., Wong, A., and Saalfeld, S. (2016). Robust registration of calcium images by learned contrast synthesis. In 2016 IEEE 13th International Symposium on Biomedical Imaging (ISBI) (IEEE), pp. 1123–1126.

Cabanac, M. (1971). Physiological role of pleasure. Science *173*, 1103–1107.

Cabanac, M. (1985). Influence of food and water deprivation on the behavior of the white rat foraging in a hostile environment. Physiol. Behav. *35*, 701–709.

Campos, C.A., Bowen, A.J., Schwartz, M.W., and Palmiter, R.D. (2016). Parabrachial CGRP Neurons Control Meal Termination. Cell Metab. *23*, 811–820.

Campos, C.A., Bowen, A.J., Roman, C.W., and Palmiter, R.D. (2018). Encoding of danger by parabrachial CGRP neurons. Nature *555*, 617–622.

Chen, Y., Lin, Y.C., Kuo, T.W., and Knight, Z.A. (2015). Sensory detection of food rapidly modulates arcuate feeding circuits. Cell *160*, 829–841.

Cowley, M.A., Smith, R.G., Diano, S., Tschöp, M., Pronchuk, N., Grove, K.L., Strasburger, C.J., Bidlingmaier, M., Esterman, M., Heiman, M.L., et al. (2003). The distribution and mechanism of action of ghrelin in the CNS demonstrates a novel hypothalamic circuit regulating energy homeostasis. Neuron *37*, 649–661.

Craig, W. (1917). Appetites and Aversions as Constituents of Instincts. Proc. Natl. Acad. Sci. USA *3*, 685–688.

Davis, J.D. (1973). The effectiveness of some sugars in stimulating licking behavior in the rat. Physiol. Behav. *11*, 39–45.

Davis, J.D., and Perez, M.C. (1993). Food deprivation- and palatability-induced microstructural changes in ingestive behavior. Am. J. Physiol. *264*, R97–R103.

Davis, J.D., and Smith, G.P. (1992). Analysis of the microstructure of the rhythmic tongue movements of rats ingesting maltose and sucrose solutions. Behav. Neurosci. *106*, 217–228.

de Cervantes, M. (1615/2015). Don Quixote (Digireads.com).

Geerling, J.C., and Loewy, A.D. (2006). Aldosterone-sensitive neurons in the nucleus of the solitary tract: efferent projections. J. Comp. Neurol. *497*, 223–250.

Geerling, J.C., and Loewy, A.D. (2007). Sodium deprivation and salt intake activate separate neuronal subpopulations in the nucleus of the solitary tract and the parabrachial complex. J. Comp. Neurol. *504*, 379–403.

Hebb, D.O. (2002). The Organization of Behavior (Lawrence Erlbaum Associates).

Johnson, F., and Wardle, J. (2014). Variety, palatability, and obesity. Adv. Nutr. *5*, 851–859.

Johnson, A.W., Sherwood, A., Smith, D.R., Wosiski-Kuhn, M., Gallagher, M., and Holland, P.C. (2010). An analysis of licking microstructure in three strains of mice. Appetite *54*, 320–330.

Krashes, M.J., Koda, S., Ye, C., Rogan, S.C., Adams, A.C., Cusher, D.S., Maratos-Flier, E., Roth, B.L., and Lowell, B.B. (2011). Rapid, reversible activation of AgRP neurons drives feeding behavior in mice. J. Clin. Invest. *121*, 1424–1428.

Kuan, L., Li, Y., Lau, C., Feng, D., Bernard, A., Sunkin, S.M., Zeng, H., Dang, C., Hawrylycz, M., and Ng, L. (2015). Neuroinformatics of the Allen Mouse Brain Connectivity Atlas. Methods *73*, 4–17.

Lee, S., Augustine, V., Zhao, Y., Ebisu, H., Ho, B., Kong, D., and Oka, Y. (2019). Chemosensory modulation of neural circuits for sodium appetite. Nature *568*, 93–97.

Leib, D.E., Zimmerman, C.A., Poormoghaddam, A., Huey, E.L., Ahn, J.S., Lin, Y.C., Tan, C.L., Chen, Y., and Knight, Z.A. (2017). The Forebrain Thirst Circuit Drives Drinking through Negative Reinforcement. Neuron *96*, 1272–1281.e4.

Li, M.M., Madara, J.C., Steger, J.S., Krashes, M.J., Balthasar, N., Campbell, J.N., Resch, J.M., Conley, N.J., Garfield, A.S., and Lowell, B.B. (2019). The Paraventricular Hypothalamus Regulates Satiety and Prevents Obesity via Two Genetically Distinct Circuits. Neuron *102*, 653–667.e6.

Lo, L., and Anderson, D.J. (2011). A Cre-dependent, anterograde transsynaptic viral tracer for mapping output pathways of genetically marked neurons. Neuron *72*, 938–950.

Magnus, C.J., Lee, P.H., Bonaventura, J., Zemla, R., Gomez, J.L., Ramirez, M.H., Hu, X., Galvan, A., Basu, J., Michaelides, M., and Sternson, S.M. (2019). Ultrapotent chemogenetics for research and potential clinical applications. Science *364*, eaav5282.

Mandelblat-Cerf, Y., Ramesh, R.N., Burgess, C.R., Patella, P., Yang, Z., Lowell, B.B., and Andermann, M.L. (2015). Arcuate hypothalamic AgRP and putative POMC neurons show opposite changes in spiking across multiple timescales. eLife *4*, e07122.

McElvain, L.E., Friedman, B., Karten, H.J., Svoboda, K., Wang, F., Deschênes, M., and Kleinfeld, D. (2018). Circuits in the rodent brainstem that control whisking in concert with other orofacial motor actions. Neuroscience *368*, 152–170.

O'Connor, E.C., Kremer, Y., Lefort, S., Harada, M., Pascoli, V., Rohner, C., and Lüscher, C. (2015). Accumbal D1R Neurons Projecting to Lateral Hypothalamus Authorize Feeding. Neuron *88*, 553–564.

Oka, Y., Ye, M., and Zuker, C.S. (2015). Thirst driving and suppressing signals encoded by distinct neural populations in the brain. Nature *520*, 349–352.

Pnevmatikakis, E.A., and Giovannucci, A. (2017). NoRMCorre: An online algorithm for piecewise rigid motion correction of calcium imaging data. J. Neurosci. Methods *291*, 83–94.

Saper, C.B., Chou, T.C., and Elmquist, J.K. (2002). The need to feed: homeostatic and hedonic control of eating. Neuron *36*, 199–211.

Shin, J.W., Geerling, J.C., Stein, M.K., Miller, R.L., and Loewy, A.D. (2011). FoxP2 brainstem neurons project to sodium appetite regulatory sites. J. Chem. Neuroanat. *42*, 1–23.

Shipley, M.T., Fu, L., Ennis, M., Liu, W.L., and Aston-Jones, G. (1996). Dendrites of locus coeruleus neurons extend preferentially into two pericoerulear zones. J. Comp. Neurol. *365*, 56–68.

Sommer, C., Straehle, C., Koethe, U., and Hamprecht, F.A. (2011). Ilastik: Interactive learning and segmentation toolkit. In 2011 IEEE international symposium on biomedical imaging: From nano to macro (IEEE), pp. 3099–3107.

Sørensen, L.B., Møller, P., Flint, A., Martens, M., and Raben, A. (2003). Effect of sensory perception of foods on appetite and food intake: a review of studies on humans. Int. J. Obes. Relat. Metab. Disord. *27*, 1152–1166.

Spector, A.C., Klumpp, P.A., and Kaplan, J.M. (1998). Analytical issues in the evaluation of food deprivation and sucrose concentration effects on the microstructure of licking behavior in the rat. Behav. Neurosci. *112*, 678–694.

Sternson, S.M., and Eiselt, A.K. (2017). Three Pillars for the Neural Control of Appetite. Annu. Rev. Physiol *79*, 401–423.

Taha, S.A., Katsuura, Y., Noorvash, D., Seroussi, A., and Fields, H.L. (2009). Convergent, not serial, striatal and pallidal circuits regulate opioid-induced food intake. Neuroscience *161*, 718–733.

Wassum, K.M., Ostlund, S.B., Maidment, N.T., and Balleine, B.W. (2009). Distinct opioid circuits determine the palatability and the desirability of rewarding events. Proc. Natl. Acad. Sci. USA *106*, 12512–12517.

Wiesenfeld, Z., Halpern, B.P., and Tapper, D.N. (1977). Licking behavior: evidence of hypoglossal oscillator. Science *196*, 1122–1124.

Winnubst, J., Bas, E., Ferreira, T.A., Wu, Z., Economo, M.N., Edson, P., Arthur, B.J., Bruns, C., Rokicki, K., Schauder, D., et al. (2019). Reconstruction of 1,000 Projection Neurons Reveals New Cell Types and Organization of Long-Range Connectivity in the Mouse Brain. Cell *179*, 268–281.e13.

Yeomans, M.R. (1998). Taste, palatability and the control of appetite. Proc. Nutr. Soc. *57*, 609–615.

Zhou, P., Resendez, S.L., Rodriguez-Romaguera, J., Jimenez, J.C., Neufeld, S.Q., Giovannucci, A., Friedrich, J., Pnevmatikakis, E.A., Stuber, G.D., Hen, R., et al. (2018). Efficient and accurate extraction of in vivo calcium signals from microendoscopic video data. eLife *7*, e28728.

Zimmerman, C.A., Lin, Y.C., Leib, D.E., Guo, L., Huey, E.L., Daly, G.E., Chen, Y., and Knight, Z.A. (2016). Thirst neurons anticipate the homeostatic consequences of eating and drinking. Nature *537*, 680–684.

STAR★METHOD

KEY RESOURCES TABLE

REAGENT or RESOURCE	SOURCE	IDENTIFIER
Antibodies		
Anti-CFOS	Cell signaling	Cat# 2250; RRID: AB_2247211
Anti-AGRP	Neuromics	Cat# GT15023; RRID: AB_2687600
Anti-GFP	Invitrogen	Cat# A-11122; RRID: AB_221569
Anti-TH	Millipore	Cat# AB152; RRID: AB_390204
In situ Probes		
Mm-Slc17a6	ACDbio	Cat# 319171-C2
Mm-Slc32a1	ACDbio	Cat# 319191-C3
tdTomato	ACDbio	Cat# 317041-C2
Virus		
HSV-hEf1α-FLEX-rev-tdTomato	Caltech	N/A
rAAV2/1-Syn-FLEX-rev-GCaMP6f	Janelia	N/A
rAAV2/2-Ef1α-FLEX-rev-ChR2-EYFP	UNC Vector Core	N/A
rAAV2/1-Ef1α-FLEX-rev-ChR2-EYFP	UNC Vector Core	N/A
rAAV2/2-Syn-FLEX-rev-PSAM4-GlyR	Janelia Vector Core	N/A
rAAV2/2-CAG-FLEX-rev-ArchT-EYFP	UNC Vector Core	N/A
rAAV2/2-CAG-FLEX-rev-ArchT-tdTomato	UNC Vector Core	N/A
rAAV2/5-Ef1a-DIO-EYFP	UPenn Vector Core	N/A
rAAV(DJ) CMV-DIO-eGFP-2A-TeNT	Stanford Vector Core	N/A
Chemicals, Peptides, and Recombinant Proteins		
Isoflurane	VEDCO	ISOSOL
Ketoprofen	Zoetis	KETOFEN
Buprenorphine	Reckitt Benckiser	Buprenex injection
Silicone gel	DOW	DOWSIL 3-4680
Dental cement	Dentsply Caulk	Self-adhesive resin cement
Silicone Elastomer	Word Precision Instruments	Kwik-Sil
Hardset mounting medium	Vectashield	H-140, DAPI containing
UV glue	Norland optical adhesive	Cat# NOA-81
uPSEM 792 hydrochloride	TOCRIS	Cat# 6865
Experimental Models: Organisms/Strains		
Agrp-IRES-Cre mice	Jackson lab	Stock 021899
Nos1-IRES-Cre mice	Jackson lab	Stock 017526
Vglut2-(Slc17a6)-IRES-Cre mice	Jackson lab	Stock 028863
Gad2-IRES-Cre mice	Jackson lab	Stock 010802
Sim1-Cre mice	Jackson lab	Stock 006451
Software and Algorithms		
MATLAB	Mathworks	https://www.mathworks.com/products/matlab.html
Jupyter	Jupyter	https://jupyter.org/
Ilastik	Ilastik	https://www.ilastik.org/
ANTs registration toolkit	Avants et al., 2011	https://github.com/ANTsX/ANTs
Fiji	ImageJ	https://imagej.net/Fiji
Bigwarp	Bogovic et al., 2016	https://github.com/saalfeldlab/bigwarp

(*Continued on next page*)

Continued

REAGENT or RESOURCE	SOURCE	IDENTIFIER
Semi-automatic slice-to-volume Brain Aligner (SBA)	This paper	https://github.com/gnayuy/braincellcount
Inscopix nVista HD	Inscopix	https://support.inscopix.com/software
iSpy	iSpy	N/A
NoRMCorre	Pnevmatikakis and Giovannucci, 2017	https://github.com/flatironinstitute/NoRMCorre
CNMF-E	Zhou et al., 2018	https://github.com/zhoupc/CNMF_E
Graphic State	Coulbourn Instruments	N/A
LabVIEW	National Instruments	N/A
Cheetah	Neuralynx	N/A
SigmaPlot	Systat software	https://systatsoftware.com/products/sigmaplot/
Arduino	Arduino	https://www.arduino.cc/en/main/software
Other		
GRIN lens	Inscopix	6.1 mm, diameter: 500 μm
Polyimide tubes for GRIN lens	Vention	Diameter: 100 μm
Tungsten wires	A-M systems	715000
Miniature microscope	Inscopix	nVista HD and HD v2
Motorized micromanipulator	MPI	SU-MPC385
Top-mounted camera	Basler	acA640-120um - Basler ace (106223)
Food pellet dispenser	Coulbourn Instruments	Grain feeder
Behavior chamber	Coulbourn Instruments	N/A
Grain pellets	TestDiet	20 mg
Sugar pellets	TestDiet	20 mg
Ensure	Abbott	Vanilla flavor
Fiber launch	Thorlabs	PAF-X-Z-A
TissueFaxs 200 (slide scanner)	Tissuegnostics	https://www.tissuegnostics.com/
Pannoramic 250 Flash III (slide scanner)	Pannoramic	N/A

RESOURCE AVAILABILITY

Lead Contact

Further information and requests for resources and reagents should be directed to and will be fulfilled by the Lead Contact, Dr. Scott M. Sternson (sternsons@janelia.hhmi.org).

Materials Availability

This study did not generate new unique reagents.

Data and Code Availability

The data and custom code that support the findings from this study are available from the Lead Contact upon request. Code used in this paper for 2D registration of the brain slice images from the whole brain are available at https://github.com/gnayuy/braincellcount.

EXPERIMENTAL MODEL AND SUBJECT DETAILS

Mice

Experimental protocols were conducted according to U.S. National Institutes of Health guidelines for animal research and were approved by the Institutional Animal Care and Use Committee and Institutional Biosafety Committee at Janelia Research Campus. Animals were housed on a 12-h light (06:00)/dark (18:00) cycle (except for imaging and closed-looped perturbation experiments, which were housed with reverse light cycle) with *ad libitum* access to water and mouse chow (PicoLab Rodent Diet 20, 5053 tablets, TestDiet). Both adult (age 8-24 weeks) male and female mice were used in similar numbers from the following Cre recombinase-expressing mouse lines: *Agrp-IRES-Cre* (Jackson lab stock 012899), *Nos1-IRES-Cre* (Jackson lab stock 017526),

Vglut2-(Slc17a6)-IRES-Cre (Jackson lab stock 028863), *Gad2-IRES-Cre* (Jackson lab stock 010802), and *Sim1-Cre* (Jackson lab stock 006451). Mice used in chemogenetic experiments (PSAM^4-GlyR mice and the corresponding EYFP control mice) were group housed. Mice used in optogenetic perturbation or imaging experiments were singly housed.

Experimental *Vglut2-IRES-Cre* mice used in chemogenetic neuromodulation for grain pellet consumption were also used for sucrose pellet consumption and water consumption (Figures 2C, 2D, and S2D). The contingent, noncontingent, and sham optogenetic perturbations were performed with the same mice (Figures 6, 7, S6E–S6J, and S7). The two palatability-shift consumption preference experiments in Figures 7J–7N were performed with the same groups of mice. The same group of mice reported in Figures S6C and S6D were tested for both place preference and contingent or non-contingent optogenetic perturbation paradigms for diluted Ensure consumption. Mice used for calcium imaging were tested in multiple different consumption experiments reported in Figures 3, 4, and 5.

METHOD DETAILS

Anatomical definition

The periLC is defined as the region within and surrounding the LC in the portion of the dorsolateral PCG that is flanked laterally by the MEV, medially by the LDT, and dorsally by the fourth ventricle (Figure S1H). It also includes a subdomain called the pre-locus coeruleus (preLC), which is defined as rostral to the LC, receiving dense axon input from HSD2 neurons from the nucleus of the solitary tract, and including neurons activated by salt deficit (Geerling and Loewy, 2006, 2007; Shin et al., 2011). We used the term periLC because it was more general, not being defined as specifically associated with salt deficit (Geerling and Loewy, 2006, 2007; Shin et al., 2011). Our study focused on the anterior periLC, and we also included glutamatergic (non-noradrenergic) anterior LC neurons in our definition of this area.

Definitions for brain region abbreviations: OLF olfactory area; HPF hippocampus formation; CTXsp cortical subplate; CNU cerebral nuclei (striatum and pallidum); TH thalamus; HY hypothalamus; MB midbrain; HB hindbrain; PT paratenial nucleus; LGv ventral lateral geniculate; PVH paraventricular hypothalamic nucleus; LHA lateral hypothalamic area; PSTN parasubthalamic nucleus; TU tuberal nucleus; PAG periaqueduetal gray; MEV midbrain trigeminal nucleus; P pons; B Barrington's nucleus; PCG pontine central gray; LC locus coeruleus; LDT laterodorsal tegmental nucleus; SLD sublaterodorsal nucleus; scp superior cerebellar peduncles; DTN dorsal tegmental nucleus; PBN parabrachial nucleus; CB cerebellum.

Virus

Viruses with the following tilters and volumes were injected: HSV-*hEf1α*-FLEX-*rev*-tdTomato (Caltech, 100 nL in SFO or 200 nL in ARC), rAAV2/1-*Syn*-FLEX-*rev*-GCaMP6f (2.0e12 GC/mL, Janelia, 200 nL in periLC), rAAV2/2-*Ef1α*-FLEX-*rev*-ChR2-EYFP (2.6e12 GC/mL, UNC, 100 nL in SFO or 140 nL in periLC), rAAV2/1-*Ef1α*-FLEX-*rev*-ChR2-EYFP (6e12 GC/mL, UNC, 500 nL in ARC, 200nl in PVH), rAAV2/1-*Syn*-FLEX-*rev*-PSAM4-GlyR (2e12 GC/ml, Janelia, 70 nL in periLC), rAAV2/2-CAG-FLEX-*rev*-ArchT-EYFP (2e12 GC/mL, UNC, 140 nL in periLC), rAAV2/2-CAG-FLEX-*rev*-ArchT-tdTomato (2.3e12 GC/ml, UNC, 70 nL in periLC), rAAV2/5-*Ef1a*-DIO-EYFP (5e12 GC/mL, UPenn, 500 nL in ARC, 100 nL in SFO, 140 nL in periLC), rAAV(DJ) *CMV*-DIO-eGFP-2A-TeNT (TeNT: tetanus toxin Stanford, 80 nL in periLC).

Surgeries

AAV injections and optic fiber implantation

For the perturbation experiments, the virus injection and optic fiber implantation were carried out as described previously (Betley et al., 2013). Briefly, virus was injected at two depths in the periLC: A/P lambda −23% distance between bregma and lambda (−0.87 mm to −1 mm), M/L ± 0.8 mm, dorsal surface −2.7 mm/-2.8 mm; ARC: A/P -bregma −1.3 mm, M/L +0.3 mm, dorsal surface −5.95 mm/ −5.85 mm; SFO: A/P bregma −0.55 mm, M/L +0.6 mm, angle 12 degree, dorsal surface −2.35 mm/-2.45 mm; PVH: bregma −0.7 mm, M/L ± 0.15 mm, dorsal surface −4.6 mm. Optical fibers were implanted 200 μm dorsal to the virus injection sites bilaterally (DFC_200/230-0.48_3.2mm_DF1.6-FLT, Doric) in periLC. A single fiber was implanted for ARC or SFO photostimulation.

HSV injections

Cre-dependent herpes simplex virus (HSV) was injected at two depths into the ARC in *Agrp-IRES-Cre* or SFO in *Nos1-IRES-Cre* mice in an animal biosafety level 2 (ABSL-2) room using the coordinates: ARC: A/P bregma −1.3 mm, M/L +0.3 mm, dorsal surface −5.95 mm/ −5.85 mm; SFO: A/P −0.55 mm, M/L +0.6 mm, angle 12 degree, dorsal surface −2.35mm/ −2.45 mm.

HSV infection leads to adverse events and mice had limited and variable survival times, so mice were closely monitored post-injection for dehydration, lack of responsiveness, hunched posture, or pain. If an animal appeared to be dehydrated, saline with 5% dextrose was administered (1 to 3 mL, SC). Pain assessment was performed if there were signs of unresponsiveness, hunched posture, or pain. If the pain assessment score reached 4, mice were sacrificed in an ABSL-2 room by transcardial perfusion followed by histology and imaging (procedure below).

GRIN lens implantation

The GRIN lenses were modified for imaging in the periLC. Three or four equally spaced polyimide tubes (diameter: 100 μm, length: 4 mm, Vention) were attached to the GRIN lens (length: 6.1 mm, diameter: 500 μm, Inscopix) using UV glue (Norland optical adhesive). The ends of the polyimide tubes were flush with the bottom of the GRIN lens. The modified GRIN lens was put in a 50-degree oven overnight to ensure that the polyimide tubes were firmly adherent. Tungsten wires (diameter: 50 μm, A-M Systems) were prepared with lengths that were of 400 - 600 μm longer than the polyimide tubes (Figure S3A and S3B). During the surgery, the GRIN lens was targeted sterotactically (lambda −23% distance between bregma and lambda, M/L +0.8 mm, dorsal surface −2.7 mm), but the GRIN lens position was also adjusted during surgery while monitoring the fluorescence signal from the miniature microscope (nVista HD and HD v2, Inscopix). The confluence of the sagittal sinus and the transverse sinus was above the periLC, and it was fatal if it was damaged. To displace this confluence of blood vessels, the modified GRIN lens was lowered down by motorized micromanipulator (SU-MPC385, MPI) for 500 μm at a position 100-200 μm posterior to the periLC to avoid the confluence. Then the GRIN lens was slowly moved anteriorly by 100-200 μm (60 μm/min), which mechanically pushed the transverse sinus forward without breaking it. The GRIN lens was held in place (10 min) for the tissue to stabilize, after which the GRIN lens was slowly lowered (0.13 mm/min) to the targeted depth (typically an additional 2.2 mm). The slow rate of decent was used to minimize damage to the confluence. At the targeted depth, we made small adjustments (50-200 μm) to GRIN lens position in order to optimize the density of transduced neurons in the field of view (FOV) such that we could identify greater than 10 well-resolved cell bodies (typically more). The tissue under the GRIN lens was then stabilized by the prepared tungsten wires (length: 4.4 - 4.6 mm) (Figure S3A). Specifically, the tungsten wires were inserted through the polyimide tubes by forceps until the ends were flush with the top of the tubes. This ensured that the distal ends of tungsten wires extended 400-600 μm beyond the GRIN lens into the underlying tissue, thus stabilizing the brain (Figure 3B). To fix the positions of the tungsten wires, UV glue was applied to the space between the tungsten wires and the openings of the polyimide tubes that were above the skull surface. Care was taken to shield the subject's eyes with metal foil. Once the tissue was stabilized, the following procedures were performed as previously described (Betley et al., 2015). Briefly, silicone gel (DOWSIL) was applied to the exposed brain surface. After 15 min, the modified GRIN lens was fixed with white dental cement (Dentsply Caulk). A head bar was added anterior to the GRIN lens with black dental cement (Lang Dental Manufacturing), which also covered the white dental cement to avoid autofluorescence. A silicone adhesive (Kwik-Sil, World Precision Instruments) was applied above the parafilm covering the lens. The field of view (FOV) was checked one month after surgery. Once the FOV was clear and contained at least 20 cells (although typically more), the baseplate was mounted for imaging experiments.

Photostimulation *in vivo*

For *in vivo* ChR2 photostimulation experiments, the pulse protocol was: 10 ms pulses, 20 pulses for 1 s, repeated every 4 s. 473 nm light output at the fiber tip was within 10 – 15 mW.

For closed-loop place preference in ArchT mice, 532 nm light was triggered on at the combined power of 7-14 mW (bilateral) at the fiber tip when mice entered the paired inhibition chamber. For *in vivo* nose poke and closed-loop consumption experiments, 532 nm light was triggered on for 10 s upon active nose poke or lick respectively at the combined power of 10 – 14 mW (bilateral) at the fiber tip.

Fos-mapping

Mice with implanted optic fiber and ChR2 expression in ARC or SFO were prepared at least two weeks before the experiments. *Agrp-IRES-Cre* mice were evaluated for evoked feeding while *Nos1-IRES-Cre* mice were tested for evoked dinking. We determined the behavioral effect of photostimulation in the light period (1 h for feeding, 0.5 h for drinking) when mice usually eat or drink little. To screen for mice with correct viral targeting and fiber placement, mice that showed evoked food consumption (> 0.6 g within 1 h) or water consumption (> 200 licks within 0.5 h) during photostimulation were selected for the subsequent Fos-mapping experiment.

The selected mice were kept overnight in the same chamber used for optical stimulation with food and water available. The optic fiber was tethered to the mouse at least 3 h before photostimulation to minimize Fos expression associated with manual handling. The food port and water port were disabled, and access was prevented from the experiment room to avoid disturbances (mice did not eat or drink during or after photostimulation for the Fos-mapping experiments). Photostimulation was delivered for 10 or 20 min by remote control (9:00 AM) and mice were sacrificed by transcardial perfusion 1.5 h post-stimulation. EYFP control mice went through the same habituation and photostimulation process as ChR2-expressing mice.

Histology and Imaging

For histology, mice were transcardially perfused with 4% paraformaldehyde in 0.1 M phosphate buffer fixative (PFA, pH 7.4). Tissues were post-fixed (3–4 h) and washed overnight in phosphate buffered saline (PBS, pH 7.4). Brain slices were sectioned by vibratome (50 μm, Leica, vt1200s).

For the whole brain mapping, the entire brain was sectioned and slices (1 in every 4) were selected for subsequent processing. Sections from the Fos-mapping groups were incubated (4°C, 48 h) with Fos primary antibodies diluted in PBS supplemented with BSA (1%) and Triton X-100 (0.1%). Brain slices from *Nos1-IRES-Cre* mice injected with virus rAAV2/2-*Ef1α*-FLEX-*rev*-ChR2-EYFP in SFO were incubated for both AGRP and GFP primary antibodies to search for AGRP and SFO^{NOS1} axon projection regions. For sections with ChR2-EYFP expression in PVH from *Sim1-IRES-Cre* mice, they were immunostained to amplify the EYFP signals in

the projection sites. Selected sections were mounted onto microscope slides with hardset mounting medium (DAPI containing, Vectashield, H-1400). Brain sections were automatically imaged using slide scanner microscopes (Panoramic 250 or TissueFaxs 200).

Primary antibodies used in this study were anti-CFOS (1:1000, Cell signaling, lot-2250), anti-AGRP (1:5000, Neuromics, GT15023), anti-GFP (1:1000, Invitrogen, A-11122), anti-TH (1:1000, Millipore, AB152). Brain sections were incubated with primary antibody (4°C) overnight for all antibodies except anti-Fos. Minimally cross-reactive fluorophore-conjugated secondary antibodies (1:500, Jackson lab) was used at room temperature (2 h). For *in situ* hybridization, RNase-free solutions were used. The protocol was from RNAscope FISH protocol in ACDbio. *In situ* probes used in this study: Mm-Slc17a6 (ACDbio, Lot-319171-C2), Mm Slc32a1 (ACDbio, Lot-319191-C3), tdTomato (ACDbio, Lot-317041-C2). For sections containing both immunostaining and *in situ* hybridization, *in situ* hybridization was performed first.

Single neuron reconstruction visualization

Single neuron reconstruction data were downloaded from http://ml-neuronbrowser.janelia.org/. Analysis and visualization of these data used the pipeline from https://github.com/MouseLightProject/ (Winnubst et al., 2019). Briefly, neurons with axon ends in PCG were selected and imported through custom MATLAB script together with the mask of brain regions (PCG, LDT, LC, B, SLD and MEV). Visualization was performed in Blender (2.8). Neurons shown in Figures 1H–1K are AA0128 (Figure 1H), AA0081 (Figure 1I), AA0167 (Figure 1J) as well as AA0761, AA0486, AA0779, AA0204, AA0177 and AA0537 (Figure 1K).

Calcium imaging in freely moving mice

Mice used in the imaging experiment were kept on a reversed light cycle (12-h light (21:00) / dark (9:00)) starting at least one week before the experiment and were behaviorally tested during the dark phase. Mice with baseplate and attached miniature microscope (nVista 2.0, Inscopix) were acclimated to the imaging behavior chamber (29 cm × 29 cm) at least two days before the imaging sessions. Calcium imaging was performed at 10 Hz frame rate and with LED power as 10%–35%. These parameters were kept the same for each mouse across all sessions. Animal behavior was recorded by a top-mounted camera (30 Hz, Basler). The synchronization signal between the miniature microscope, top-mounted camera, and behavior-related events (cue, lick and pump events) was recorded either by a signal acquisition system (Neuralynx) or by a custom Arduino board.

Food, false food, social interactions, ghrelin injection

Grain food pellets (identical to those in the homecage), false food (wood block with similar color and shape as grain pellets), or another mouse (opposite sex) were placed into the chamber 60 - 90 s after onset of imaging sessions in food deprived mice. These items were removed after approximately 1 min. Ghrelin (1 μg/g) or saline (the same volume as ghrelin) were injected (i.p.) in *ad libitum* fed mice. Neuron dynamics were recorded over multiple imaging trials (around 3 min) with 10-min inter-trial intervals.

Cue-conditioned consumption

For conditioned consumption of liquids (Ensure, liquid food, water), a 200 ms auditory cue (12 kHz) was randomly presented in every 30-40 s after onset of the imaging sessions. The lickometer spout was extended by stepmotor to the food port 800 ms after the auditory cue, which is a time delay that was used previously for identifying cue-dependent modulation of AGRP neurons (Betley et al., 2015). Once a lick was detected by the capacitive sensor attached to the lickometer spout, a quantity (3 μL) of liquid food, Ensure. water, or taste solutions was pushed out by a pump that held the liquid-containing syringe (Figure 3C). The spout was withdrawn 5 s after extension unless stated otherwise.

For the liquid food, water, or tastant consumption trials, mice went through 24 h food deprivation or water restriction before the imaging sessions (Figures 3E and 3F). For the trials with different consumption times, the lickometer spout was extended and withdrawn automatically using the stepmotor (Figures 3J and 3K), and every three licks triggered delivery of 3 uL of food within the access time.

For the cell-matched comparison of neurons to Ensure in hunger and water in thirst (Figure S3I), FD mice first performed conditioned Ensure consumption, followed by free-access consumption of low hydration grain pellets (1 h) to make them thirsty, and then they performed cue-conditioned water consumption trials.

When comparing the cell-matched responses in mice transitioned from hunger → satiety or thirst → satiety, conditioned consumption trials were interleaved with self-paced consumption trial to allow FD or WD mice to reach a satiated state (Figures 4K–4P, see below). We considered mice to be in a satiety state when mice showed a substantial number of misses during the conditioned consumption trials and also showed consistently low bout duration in self-paced consumption trials (Figure S3L).

When comparing the ensemble activity changes between energy balance states (Figures S4K and S4L), two-successive-day imaging experiments were performed with the first day as mice under *ad libitum* fed and the second after 24 h food deprivation (Figures S4K and S4L).

Self-paced consumption

Mice under FD had free access to Ensure via the lickometer spout for 2-5 min in each self-paced consumption trial. These trials were interleaved with multiple cue-conditioned consumption trials in which mice consumed a small volume (3 μL) of Ensure, as described

above (Figures 3L–3O). To classify neurons as significantly activated or significantly inhibited, we used the Wilcoxon signed-rank test for the cue-conditioned trials. Each self-paced consumption trial usually contained multiple consumption bouts (defined for this analysis as continuous licking with an inter-lick-interval less than 1 s). The neuronal dynamics of periLC^{VGLUT2} neurons were then analyzed for their relationship to bout duration.

Taste coding by periLC^{VGLUT2} neurons

For consumption of different tastes, three small lickometer spouts (outer diameter: 1.05 mm; inner diameter: 0.5 mm) soldered together replaced the single lickometer spout in Figure 3C. These three lickometer spouts were separately connected to syringes loaded with either water or one of the two different tastes, which were independently controlled by three pumps. Consumption of two different tastes was examined within each session. Between trials with different tastes, water flushed the lickometer spout-tips (at least 100 μL) to prevent tastant contamination. Each continuous imaging trial was around 5 min and usually contained 3 to 5 cue-conditioned consumption trials. Mice in this study went through 8-20 imaging trials in one session (day) depending on their need state.

Mice were kept on water restriction for the taste consumption trials with daily health monitoring and body weight assessments. Only 3 uL of tastants were given in each cue-conditioned trial for WR mice to guarantee consistent consumption of the volume across tastants. During water restriction, mice received 1 mL water daily, including the solutions received in the imaging sessions and water supplied afterward in the homecage. Restriction was eased if mice fell below 70% of their initial *ad libitum* fed body weight or failed quantitative health assessment.

Neuron perturbations during behavior

Behavioral experiments involving neuron perturbations were performed in sound attenuating chambers.

Chemogenetic or optogenetic modulation of food or water intake

Mice had *ad libitum* access to food and water, and test sessions were performed in the light period for food and water intake experiments. For food intake experiments, mice with periLC^{VGLUT2} neurons expressing PSAM^4-GlyR-IRES-EGFP or EYFP control mice were acclimatized (12 h) to behavior cages equipped with an automated food pellet dispenser (Coulbourn Instruments). Saline, uPSEM^{792} (1 mg/kg in saline), uPSEM^{792} (3 mg/kg), and saline were injected (i.p.) over the next four consecutive days. Food and water consumption (2 h) were monitored using Graphic State (Coulbourn Instruments). Standard grain and sugar pellets (20 mg, TestDiet) were used as the food sources. Sugar pellets were much harder than grain, which may account for less consumption than grain pellets in this study.

Ad libitum fed mice expressing ChR2 in periLC^{VGLUT2} neurons had at least two-day habituation in that chamber to get used to palatable liquid food (Ensure, Abbott) consumption. A customized behavior chamber (29 cm × 29 cm) with a slot for a lickometer spout to be automatically extended by stepmotor was used for the perturbation assay. Ensure contained in a syringe was delivered through tubing connected to the lickometer spout. The capacitive sensor was attached to the lickometer spout and every 3 licks triggered the pump to deliver 3 μL Ensure. Mice had free access to Ensure consumption without any perturbation (30 min) on the first day and received photostimulation (30 min) on the second day. Lick events were recorded continuously by an Arduino board throughout the session.

Conditioned Place Preference

A two chambered apparatus was used as described previously (Betley et al., 2015). *Ad libitum* fed mice were acclimatized to the apparatus on the first day. On the second day, pre-test preference score was determined after mice were allowed to freely explore in the apparatus. Over the next four days, a 532 nm laser was triggered when periLC^{VGLUT2} ArchT mice entered the initially less preferred chamber while 473 nm photostimulation was given when periLC^{VGLUT2} ChR2 mice enter the initially more preferred side. Mice were then given free access to both chambers without any perturbation on the test day. If the time spent in the conditioned chamber reached 100% before the fourth conditioning session, mice were allowed to directly go to the test session on the next day. Each session lasted 15 min and optic fibers were always tethered, even for test days without optical perturbation. A camera installed above the apparatus (30 Hz, Basler) tracked mouse position throughout the session.

Nose poke experiment

A matte white (to avoid reflections) customized apparatus (29 cm × 29 cm) with two identical poke holes (W × H: 1.5 cm × 2.0 cm) separated 4.2 cm apart was used for the nose-poke experiment. PeriLC^{VGLUT2} ArchT mice tethered with an optical fiber freely explored this apparatus (1 h). Infrared beam sensors were installed at the sides of the poke holes. A beam break detected by the sensor in the active poke hole triggered 532 nm laser. There was no consequence from nose-poking the inactive port. Active and inactive poke holes were randomly determined for each mouse. Mice were given one session to show nose poke behavior. The beam break and laser pulse events throughout the session were monitored by a custom Arduino board.

Quinine and Ensure consumption

Vglut2-IRES-Cre mice injected with AAV vectors expressing TetTox-EYFP or EYFP were allowed to express for one month before the consumption experiment. Mice were acclimated to the taste-delivery behavior chamber (29 cm × 29 cm) for at least 2 days. Diluted

Ensure (1:4) or quinine (1 mM) were delivered through the lickometer spout (3 μL) with three interleaved sessions for each. Each session was 0.5 h, with one session per day.

Closed-loop food intake and water intake experiment

Behavior chamber and liquid-food delivery setup were as described above for the closed-loop food and water intake experiment. 532nm laser (SLOC) was aligned to the shutter (Uniblitz), which controlled laser light delivery to the mouse brain via a fiber launch (PAF-X-Z-A, Thorlabs). A relay box controlled the shutter opening, which had two dependencies: information about the experimental block (laser-on or laser-off) from Arduino Board I and lick events (for contingent and sham conditions, see below) or pseudo-events information (for noncontingent photoinhibition, see below) from Arduino Board II (Figure 6A). Arduino Board I sent out a signal representing the block identity to the relay box, which determined the laser-on and laser-off blocks. Arduino Board II recorded mouse licks detected by the capacitive sensor. In the noncontingent photoinhibition sessions, Arduino Board II generated pseudo-event signals (see below) to the relay box to randomly open the shutter in the laser-on blocks. In the lick-contingent and sham sessions, licks recorded by Arduino Board II triggered an event signal delivered to the relay box that opened the shutter in laser-on blocks. During the laser-off blocks, signals from the lick-sensor were recorded but did not open the shutter. In sham photoinhibition sessions, the shutter was engaged as with lick-contingent conditions but the laser was not on.

Mice had free access to diluted Ensure (1:4) or water in the chamber during the consumption sessions. The whole session was divided into alternate laser-off blocks and laser-on blocks (Figure 6B). For diluted Ensure consumption sessions (2 h), block duration was 2 min. For water consumption sessions (1 h), block duration was 1 min.

Circadian rhythm reversed (light 21:00 / dark 9:00) periLC^{VGLUT2} ArchT mice that had *ad libitum* food went through at least five days to acclimate to Ensure consumption before closed-loop perturbation in their dark phase. Over the first two days, mice had free access to undiluted Ensure consumption in the same chamber used for closed-loop perturbation (1 h/day). Mice whose Ensure consumption reached 900 licks/h were then acclimated to diluted Ensure (1:4) consumption over the next three days (1 h/day). For mice with undiluted Ensure consumption less than that criteria, one more Ensure consumption session was given next day. Mice with total licks above 600 licks/h in diluted Ensure consumption were selected for subsequent experiments. Sessions of contingent paradigms, sessions of noncontingent paradigms and sessions of sham paradigms were performed over consecutive days. For each mouse, the noncontingent conditions delivered the same number of shutter openings as were determined in the contingent experiments by preprogramming these as pseudo-events with random inter-event-intervals within the laser-on blocks. In this way, mice experienced the same exposure to photoinhibition, but it was independent of lick events. This is equivalent to open-loop perturbation with the same inhibition time as the lick-contingent closed-loop sessions. In the water intake experiment, mice were under water restriction and 600 μL water was given 15 min before the sessions to reduce thirst, which avoided a ceiling effect for water consumption motivation. The total water received by these mice was 1 mL per day, including water received before the sessions, during the sessions, and supplied in the homecage afterward. Behaviors were recorded by the top camera (30 Hz, Basler) throughout the session and all the lick, block, and inhibition pulse events were recorded synchronously.

Two bottle preference test

A behavior chamber with two water bottles was used (Coulbourn Instruments). Capacitive detectors were linked to the lick spout of the bottle to record lick events and send signals to trigger laser pulses, which was controlled by Labview. For experiments with identical sucralose concentration, two identical bottles containing sucralose solutions (0.5 mM) in water were placed at the left and right sides of the chamber. The starting photoinhibition side was less-preferred side. For experiments with different sucralose concentrations, one bottle contained 0.25 mM sucralose and the other contained 0.5 mM sucralose solutions, which were available simultaneously. Left and right position of the different solutions were counterbalanced across mice.

Circadian rhythm reversed (light 21:00 / dark 9:00) periLC^{VGLUT2} ArchT or EYFP mice that had *ad libitum* food and water went through at least two days to acclimate to the behavior chamber using a 300 mM sucrose supply for 1 h each day. Fibers were tethered on the second day. Mice whose sucrose consumption was above 200 licks within the second session were used for the subsequent experiments with non-caloric sucralose consumption.

First, mice went through the preference test using identical sucralose concentrations (0.5 mM). On the first day, preference score calculated as (A - B) / (A + B), (where A and B are the total licks on either side) was determined based on consumption from both spouts in the absence of photoinhibition. On the second day, a 532 nm laser was triggered on for 10 s when mice licked the initially less preferred spout. The third day, the spout that triggered photoinhibition was reversed. On the subsequent extinction day, spout licking did not trigger the laser. Next, mice were tested in a different experiment using two bottles containing 0.25 mM and 0.5 mM sucralose solutions, first with pre-test in the absence of laser followed by a photoinhibition session, in which a 532 nm laser was triggered only when mice consumed the 0.25 mM sucralose solution. On the subsequent day, mice were tested in extinction with both spouts but in the absence of laser triggering. All the sessions were 1 h and performed in the mouse's dark phase.

QUANTIFICATION AND STATISTICAL ANALYSIS

2D registration and cell counting

We developed a semi-automatic Slice-to-volume Brain Aligner (SBA) to do the registration for C-Fos-IR and HSV labeling counting. The Allen Mouse Brain Reference Atlas (CCF v3.0) (Kuan et al., 2015) was used as the template. We manually matched selected key pairs of brain slices (1 in every 4) between our experimental brain data (Fos-mapping and HSV-tdTomato mapping) and 2D *CCF.* These brain slices usually contained landmarks such as anterior commissure, third ventricle or hippocampus structures. Therefore, these selected experimental brain slices and 2D CCF could be manually matched. If experimental brain slices were tilted, 3D CCF was resliced to 2D CCF with the same angle of the experimental data. All the matching pairs between experimental brain slices and 2D CCF were determined by linear curve fit based on the above manually selected key pairs. All these pairs were checked manually to ensure accuracy before the registration. Affine and diffeomorphic registration were applied to find non-rigid transformations between each pair of 2D brain slices using the ANTs registration toolkit (Avants et al., 2011). For sections that were broken during immunostaining or mounting, registration was first carried out using Bigwarp (FIJI) (Bogovic et al., 2016), followed by ANTs to refine the registration. CCF annotation templates were warped onto experimental slices for labeling quantification (Figure S1D). Oppositely, experimental slices were warped to the CCF annotation for visualization (Figure 1C). Experimental data here was down-sampled (8-fold in x-y) to avoid heavy computation during registration, and warped results were then up-sampled to original sizes for subsequent quantification.

For counting Fos-IR and tdTomato-expressing somata, rolling ball background subtraction (FIJI) was first carried out to correct background fluorescence in the scanned images. Ilastik was used for probability-based binarization and neuron segmentation (Sommer et al., 2011). Custom MATLAB scripts were used to count the labeled neurons (N) in different brain regions by referring to the corresponding warped CCF annotation templates. Data from all the brain regions was collected except a few regions due to damage during immunostaining or mounting. Relative labeling density (R) was calculated as N/Area. Area was the total pixels of the corresponding brain regions annotated in the warped CCF templates. Data was further normalized as $(R - R_{min}) / (R_{98\%} - R_{min})$ within each brain across 259 brain regions defined by Allen Mouse Brain Reference Atlas (Figure S1D). To simplify visualization, a binarized labeling map was used by applying a threshold (40%) to the relative labeling density (Figure S1E). We then took the logical intersection across all the samples from the AGRP and SFO groups (Figure 1D).

Calcium Imaging Analysis

Analysis of calcium imaging times series was performed in Fiji and MATLAB. The spatially down-sampled imaging data (2-fold in x-y) was first motion-corrected using NoRMCorre (Pnevmatikakis and Giovannucci, 2017), and then further registered with ANTs to remove nonlinear distortions (Betley et al., 2015). Registered data was further downsampled (2-fold in x-y) and smoothed by median filter in time (z radius = 5, Fiji). Constrained non-negative matrix factorization (CNMF-E) for microendoscopy was used to extract GCaMP6f fluorescence responses associated with individual neurons from the processed registered data (Zhou et al., 2018). Briefly, we estimated the background through the initialized spatial and temporal components of individual neurons at first, and then updated the spatial and temporal components based on the estimated background. We repeated this process to optimize the background, spatial, and temporal component values. Extracted data were manually inspected afterward to remove the obvious non-neural objects that had usually unrealistically small (1- 5 pixels) or large (above 100 pixels) soma sizes. In conventional calcium imaging, fluorescence signals are compared as $\Delta F/F$, where F is the fluorescence level of the neuron in the resting state. For epifluorescence imaging in the brain, F is significantly contaminated by background fluorescence fluctuations in the neuropil, which may be unrelated to the intracellular calcium concentrations of individual neurons. Thus, the inspected raw output of CNMF-E, which we called ΔF, was used for the subsequent analysis.

For analysis of neuronal dynamics across trials within a session, ΔF from all the trials was used to calculate Area under the Receiver Operating Characteristic (auROC) curve using MATLAB function 'ROC'. For the false positive rate of the ROC curve, we used the shuffled ΔF within the baseline time period (5 s) before the event (auditory cue or lick), and this was compared to the neuron dynamics response during a behavioral event (bin size 100 ms) (Figures 3D–3F, 3I, S3J, S4A, and S4D). Cell response examples were represented as z-score of ΔF (Figures 3H, 3J, 3P, S4C, and S4F), and baseline activities (mean response from −5 s to 0 s) were subtracted when time-lapse responses were shown in Figures 3M–3O, 3Q, 4L, 4M, 4O, 4P, S4B, S4E, 5B, and 5C. For the self-paced consumption trials, short and long bouts were defined according to the distribution of the normalized bout durations: short bouts were the shortest 30% of consumption bouts, and long bouts were the longest 15%. Neuronal dynamics during the short bouts were up-sampled to make the temporal sample sizes match the longest short bouts, while the long bouts were down-sampled to match the shortest long bouts. Mean responses across either short or long bouts were shown as mean z-score (Figures 3M–3O). Area under the curve (AUC) for consumption or omission trials was the sum of z-score values after baseline subtraction (Figures 3Q, 4L, 4M, 4O, 4P, 5J–5O, S5B, and S5D). The relationship between AUC and bout duration was tested with linear curve fitting (Figures 3L and S3M–S3P). For trials with different access time to Ensure, the mean response was the mean of the z-score within the consumption window after subtracting the baseline. The correlation coefficient between the calcium fluorescence response to Ensure and licks or lick frequency was calculated with MATLAB function 'corrcoef' (Figures S3Q–S3S). Statistically significant neuron dynamics responses across trials were determined by Wilcoxon signed rank test (Figures 3G, S3S, S4A, S4D, and S4N). To compare different taste responses within a session, ΔF for each neuron was averaged

across multiple trials, then the z-score was calculated from this average response, and the response was displayed after subtracting the baseline values (Figures 5D–5I). To report average fluorescence responses across neurons within a session, normalized ΔF was calculated as (ΔF - ΔF_{min}) / (ΔF_{max} - ΔF_{min}) (for a range of 0 to 1), or it was calculated as (ΔF - $\Delta F_{baseline}$) / abs (max (ΔF - $\Delta F_{baseline}$)) (for a range of −1 to 1) (Figures 3K, 4E–4J, and 5A). Linear regression was used to test normalized mean response or baseline changes across successive trials within a session under FD or WD. For this, the mean value of normalized fluorescence responses from all the neurons, the inhibited subgroup, or the activated subgroups were analyzed. In addition, linear regression was performed on individual neurons across trials (Figures 4E–4J and S4G–S4J).

When comparing the neuron dynamics from different sessions, the extracted ΔF was scaled by system noise level E, calculated through the power-spectrum density method in CNMF-E, instead of the calcium signals in the resting state. This final output was similar to z-score and called 'scaled ΔF' in this study (as suggested by the CNMF-E FAQ at https://github.com/zhoupc/CNMF_E/wiki/FAQ) (Figures S4K, S4L, and S3H). For the Ensure response under as *ad lib* fed versus FD, the session average of baseline subtracted scaled ΔF across all the trials for each neuron from the two ensembles were compared (Figures S4K and S4L). For ghrelin administration, the mean of the scaled ΔF (100 s, 10 min and 20 min post-injection) of individual neurons were compared to that at the same timescale from saline injection (Figure S3H).

Response clusters from different tastes were calculated by unsupervised k-means clustering with the mean responses from two tastes as the input. The optimal number of clusters was determined by the MATLAB function 'evalclusters' with silhouette value as the evaluation criteria (Figures 5D–5I).

For the grain food, false food, and social interaction trials or the ghrelin and saline injection trials, the behavioral events were manually marked from the synchronized behavioral video. For the other cue-conditioned consumption trials, custom MATLAB scripts were used to extract the event time out through the synchronized data collected by Neuralynx or Arduino boards.

Analysis of closed-loop perturbation behavioral experiments

All data analysis was performed with custom MATLAB scripts. Lick events in two different blocks were separately grouped to do the further analysis. Average licks / block only included the blocks in which mice initiated licking, and lick frequency was calculated by excluding the time before mice initiated licking within each block (Figures 6G and 6I). Bin size (10 s) was chosen to analyze the lick events throughout the sessions (Figures 6F, 6H, S6A, and S6I). Synchronized behavioral recording was used to analyze mouse locomotor trajectory throughout the session and the boundary of the food zone area was defined by video analysis of the mouse position when lick events were recorded and expanding this area by 5% (Figure S7B). The duration of the whole lick period within one entry into the food zone was defined as a feeding or drinking bout. To empirically define a feeding or drinking bout threshold based on mouse behavior, we measured the minimum time mice spent in the food zone while there was consumption, which was 16 s (Figure S7C). We also analyzed the data with a 1 s inter-lick interval (ILI) used for to define a feeding or drinking bout based on common practice in the literature (Johnson et al., 2010; Spector et al., 1998). Thus, both 1 s and 16 s ILI were used as the threshold to define the consumption bout in this study. ILIs above 1 s or 16 s indicated an initiation of a new bout. Bout durations in all the laser-on blocks and no-laser blocks from the same session were collected for analysis. When analyzing feeding bouts that straddled laser-on and the following laser-off blocks, we analyzed the first 15 s or 30 s and last 15 s or 30 s of the no-laser blocks that contained feeding bouts (Figures 7G and S7N).

We fit parametric probability distributions to the distribution of bout durations (defined using a 16 s threshold) in each of 12 conditions (all combinations of contingent versus no-laser, non-contingent versus no-laser, sham versus no-laser in feeding and drinking). Bouts that contained only a single lick were removed from the analysis (these can be non-consummatory contact with the spout). In each condition, we used maximum likelihood estimation (via the 'allfitdist' in MATLAB) to determine the best-fitting parameters of 16 different parametric distributions: Exponential, Gamma, Weibull, Nakagami, Generalized Pareto, Lognormal, Log-logistic, Birnbaum Saunders, Generalized Extreme Value, Inverse Gaussian, T-Location-Scale, Logistic, Normal, Rayleigh, Rician, and Extreme Value. We ranked fits according to the Bayesian Information Criterion (BIC), which is a statistic that considers both goodness-of-fit and parsimony. In 8 of 12 conditions, the exponential distribution had the lowest BIC. For the other 4 conditions, the exponential distribution was among the top 3 best-fitting distributions (see Table S3). Therefore, the exponential distribution gave the most parsimonious fit to the data. Error bars for the mean value (mean duration cluster) were calculated using the MATLAB function 'paramci', which determines the 95% confidence intervals based on a chi-square distribution (Figures 7B, 7E, 7H, and S7O). A mixture of two Gaussian distributions was fit to the distribution of ILIs less than 1 s under contingent and non-contingent conditions (Figure S7A). The five parameters that specify the Gaussian mixture distribution fit were calculated using the MATLAB function 'mle'. The statistical significance of our measured change in P_{stay} was assessed via shuffle tests. We first shuffled bouts across all blocks taken from the contingent photoinhibition session (i.e., shuffling between laser-on and laser-off blocks) and then repartitioned these bouts into two groups, followed by exponential curve refitting for each group and recalculation of ΔP_{stay} (shuffled). We repeated this shuffle procedure 1000 times and compared the distribution of ΔP_{stay} (shuffled) to the measured value (real) (Figure S7G). For both feeding and drinking, all shuffled values of ΔP_{stay} were smaller than the true value, and thus $p = 0.001$ in both cases. To illustrate the impact of the observed shifts in P_{stay} shifts, we also showed the probability of staying in a consumption state for a given duration of time (Δt_{stay}) by plotting $(P_{stay})^t$ versus Δt_{stay} for two different values of P_{stay} (Figure S7).

Statistics

Values were represented as mean ± SD unless otherwise stated. All the statistics were performed using SigmaPlot (Systat) or MATLAB. Pairwise comparisons were calculated by unpaired or paired t test for two samples and one-way repeated ANOVA for multiples samples unless the data violated normal distribution assumption, which were then calculated by nonparametric Wilcoxon signed rank test (two samples) or Friedman repeated-measures analysis of variance on ranks (multiple samples). Bonforroni-Holm (all pairwise) or Dunnett (versus control) were used to do multiple sample comparison correction. Ensemble neuron response distribution and feeding bout distribution were analyzed in the nonparametric two sample Kolmogorov-Smirnov test. When a large number of statistical comparisons were performed, P values were corrected by false discovery rate (FDR). Pearson correlation coefficient or liner regression were used to test the relationship between neuron response and lick duration, lick frequency or trials numbers respectively. Results of statistical tests were summarized in Table S1. ns $p > 0.05$, *$p < 0.05$, **$p < 0.01$, ***$p < 0.001$.

CellPress

Supplemental Figures

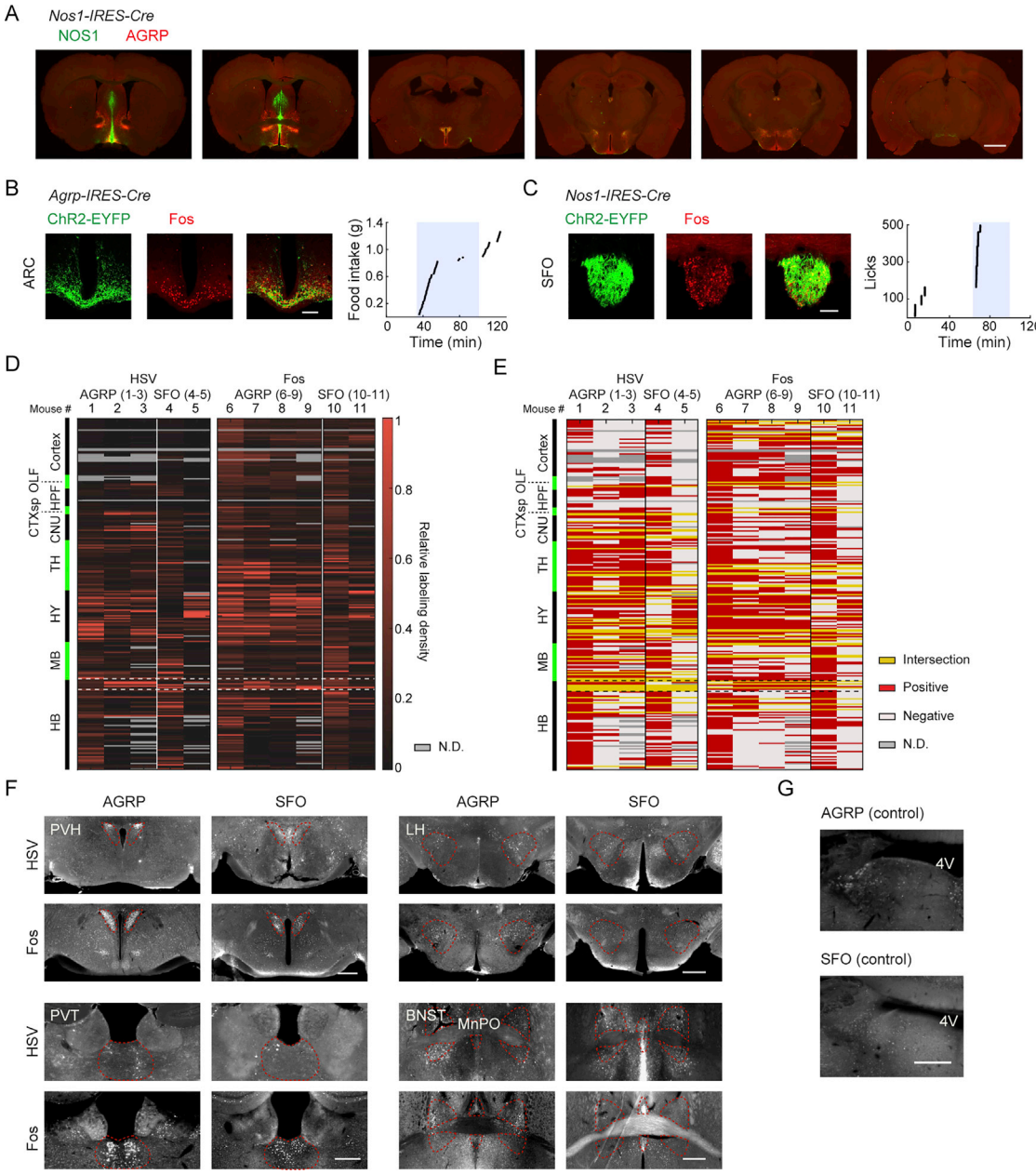

Figure S1. Convergence of Feeding and Drinking Circuits, Related to Figure 1

(A) AGRP axon immunostaining and SFO^{NOS1} neuron axon projections (ChR2-EYFP) overlap in several brain regions. Scale bar: 2 mm. (B) Example images of ChR2-EYFP expression in the ARC from an *Agrp-IRES-Cre* mouse used for Fos-mapping and corresponding food intake driven by AGRP neuron activation. Scale bar: 100 μm. Shaded area: time-period for photostimulation. (C) Example images of ChR2-EYFP expression in the SFO from a *Nos1-IRES-Cre* mouse used for Fos-mapping and corresponding water drinking driven by SFO^{NOS1} neuron activation. Scale bar: 100 μm. (D) Relative labeling density across 259 brain regions defined by the Allen Brain Reference Atlas from HSV mapping and Fos mapping for individual mice. Dashed lines denote regions in and around pontine central gray. HSV group: Mouse 1, 40 h post-infection (p.i.); Mouse 2, 3 and 5, 72 h p.i.; Mouse 4, 36 h p.i.; Fos group: Mouse 6, 7 and 10, 10 min stimulation; Mouse 8, 9 and 11, 20 min stimulation. Gray: brain regions not determined. Dashed-lines denote regions in and around PCG. Abbreviations: see STAR Methods. (E) Binarized expression for HSV-mapping and Fos-mapping for labeling density above 40th percentile shown in (D). (F) Example images of HSV-tdTomato labeling or Fos-IR in regions directly downstream of AGRP neurons or SFO^{NOS1} neurons. Dashed red line: boundary for the anatomic regions. Scale bar: 500 μm. (G) Fos-IR in PCG in control mice that lacked ChR2 in AGRP or SFO^{NOS1} neurons. Scale bar: 500 μm.

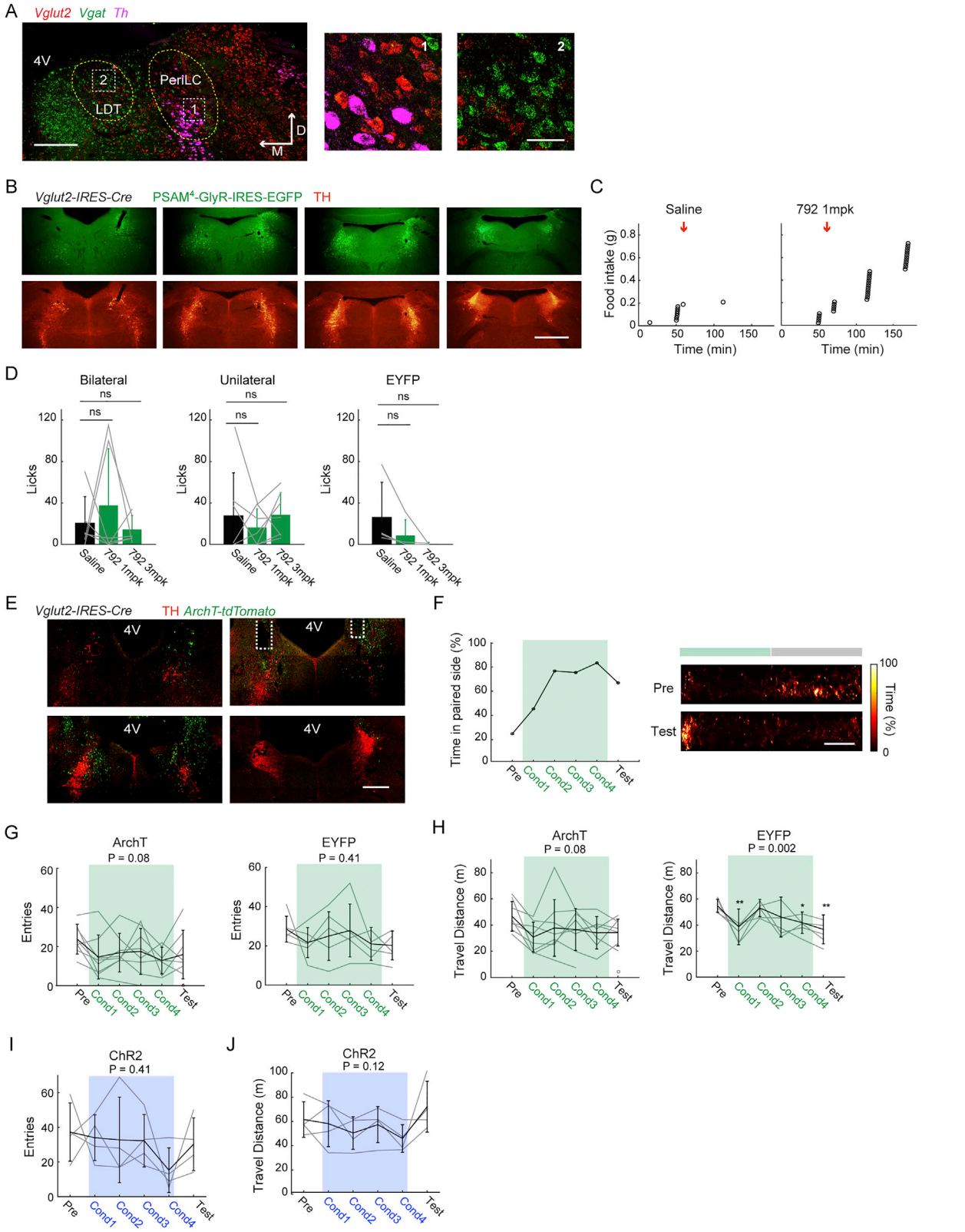

(legend on next page)

Figure S2. PeriLC^{VGLUT2} Neurons Control Food Intake and Do Not Affect Locomotion, Related to Figure 2

(A) Three-plex fluorescent *in situ* hybridization (FISH) in periLC and LDT showing that glutamatergic VGLUT2 neurons are the predominant population in periLC and GABAergic VGAT neurons are primarily in LDT, scale bar: 250 μm. Insets 1 and 2 are from periLC and LDT, scale bar: 40 μm. Red: *Vglut2*; green: *Vgat*; magenta: *Th*, M: medial, D: dorsal. (B-C) Example images of PSAM^4-GlyR-IRES-EGFP expression in periLC^{VGLUT2} neurons (B, top) along with TH-IR (B, bottom), and corresponding food intake from this mouse after injection of saline or uPSEM^{792} (C). (D) Water consumption (2 h) from mice with bilateral (n = 6) or unilateral (n = 4) PSAM^4-GlyR expression as well as EYFP controls (n = 7) after saline or uPSEM^{792} injection. (E-F) Example images of ArchT-tdTomato expression (fluorescent *in situ* hybridization, green) from a periLC^{VGLUT2} mouse along with TH-IR to mark the LC (E) and its place conditioning to the photoinhibition side (F). Scale bar: 10 cm. Dashed white rectangle: fiber position. Green shaded area: sessions for photoinhibition place conditioning. (G) Number of entries to side paired with laser for ArchT mice (n = 8) and EYFP control mice (n = 6). (H) Total travel distance of ArchT mice (n = 8) and EYFP control mice (n = 6) within 15 min sessions in conditioned place preference test. Statistical significance in control mice (right) was likely related to unusually low variability in pre-test, compared to ArchT and ChR2 (J) mice and was not systematic across conditioning days. (I-J) Number of entries to laser side (I, n = 4) and total travel distance of ChR2 mice during 15 min place preference sessions (J, n = 4). Blue shaded area: sessions for photoactivation place conditioning. Error bars: SD. ns $p > 0.05$. Statistics: Table S1.

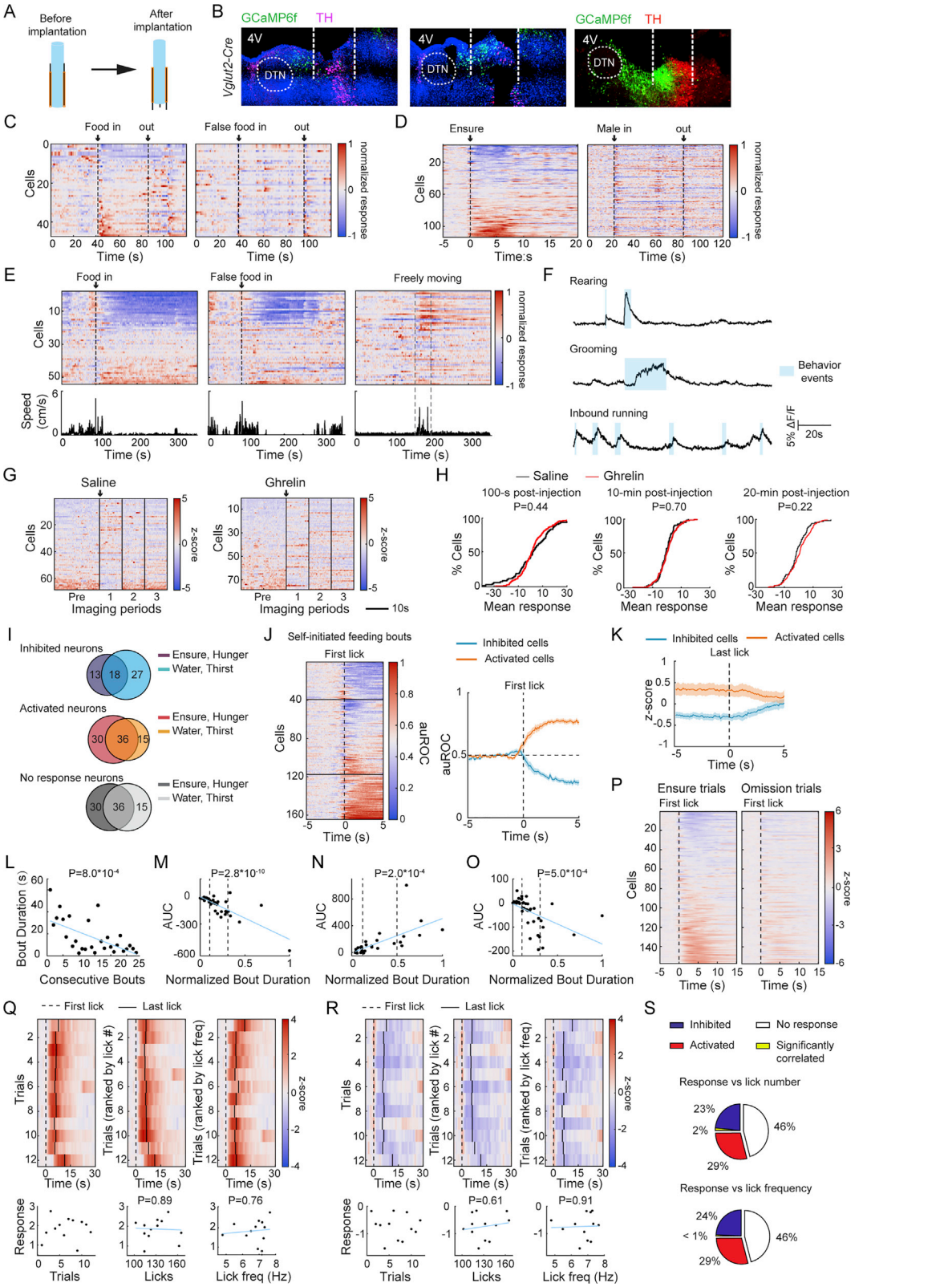

(legend on next page)

Figure S3. GABAergic and Glutamatergic Neuron Dynamics in the Dorsolateral PCG during Behavior, Related to Figure 3

(A) Modified GRIN lens uses extended tungsten wires to anchor the underlying tissue. (B) Examples of GRIN lens placement for imaging periLC^{VGLUT2} neurons. Green: GCaMP6f, magenta/red: TH, blue: DAPI, white dashed line: tungsten wire tract, 4V: fourth ventricle, DTN: Dorsal tegmental nucleus. Left side: medial, Right side: lateral. (C) Ensemble response of matched periLC^{VGLUT2} neurons to grain food pellets and a false food (wood block) under FD. (D) Ensemble response of matched periLC^{VGLUT2} neurons from a female mouse to Ensure consumption and social interaction with male mouse. (E) Ensemble response of LDT^{GAD2} neurons to food, false-food, and under free exploration conditions (top) and corresponding histogram of mouse locomotion speed (bottom). (F) Example traces from three LDT^{GAD2} neurons that show specific responses when the mouse is rearing, grooming, or inbound running (running toward the food port). (G) Ensemble response of periLC^{VGLUT2} neurons to saline or ghrelin injection. Black line: boundary for imaging trials. (H) Cumulative distribution of mean scaled ΔF responses of periLC^{VGLUT2} neurons at 100 s, 10 min, or 20 min after saline (black line) or ghrelin injection (red line). (I) Cell-matched analysis of the number of periLC^{VGLUT2} neurons that were significantly inhibited, activated, or showed no significant response to Ensure under hunger, water under thirst, and the intersection of both (n = 220 neurons, 3 mice). (J) Ensemble response of periLC^{VGLUT2} neurons during self-paced Ensure consumption trials (left, n = 164 neurons, 3 mice). Solid lines: division of significantly inhibited (upper) or activated (lower) subpopulations. Right, mean response from significantly consumption-inhibited and consumption-activated subpopulations. Dashed line: First lick. Horizontal dashed line: auROC = 0.5. Shaded area: ± SEM (K) Mean response from significantly activated and inhibited subpopulations aligned to the last lick. (L) Consumption bout duration becomes shorter across consecutive bouts during self-paced free-consumption trials with Ensure as mouse transitioned from hunger to satiated state. (M) and (N) Example cells in Figures 3M and 3N whose response magnitudes are positively correlated with feeding bout duration. (O) Example 'activated' cell from Figure 3O whose response is negatively correlated with bout duration becomes inhibited with long duration bouts. Blue line: linear least-squares fit. First dashed line: division between the short bouts and middle bouts. Second dashed line: division between the middle bouts and long bouts. (P) Ensemble response of periLC^{VGLUT2} neurons during cue-conditioned consumption trials and omission trials (n = 154 neurons, 3 mice). (Q and R) Example responses from a consumption-activated (Q) and a consumption-inhibited (R) periLC^{VGLUT2} neuron with different experimenter-controlled consumption times. These trials were sorted by consecutive trial number, number of licks, or lick frequency respectively (left to right). The mean response as a function of these parameters is shown in the bottom panels. Blue line: linear least-squares fit. (S) The proportion of activated or inhibited neurons and a small proportion whose responses are significantly correlated with number of licks or lick frequency. Statistics: Table S1.

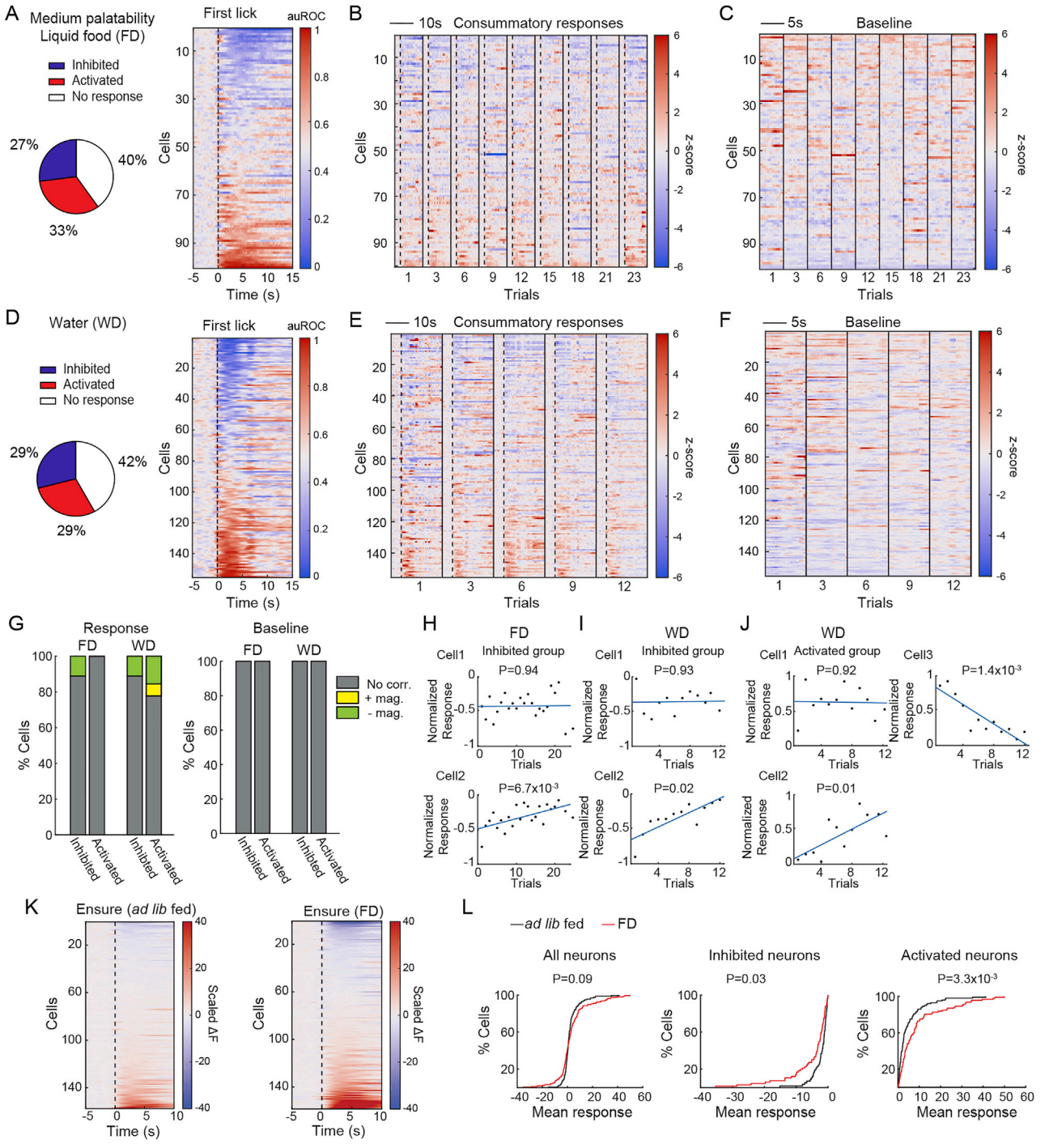

(legend on next page)

Figure S4. PeriLC^{VGLUT2} Neuron Responses to Food and Water across Multiple Trials and Food Deprivation, Related to Figure 4

(A) Proportion of significantly activated and inhibited periLC^{VGLUT2} neuron responses (left) and also ensemble response (right) to MP liquid food under FD, which is the same as Figure 3E. (B) Example liquid food responses across individual trials of the neurons shown in A. Black dash line: first lick; black solid line: divisions for trials. (C) Examples of baseline dynamics from trials shown in B. Black solid line: divisions for trials. (D-F) As in A-C for WD mice drinking water. (G) Proportion of neurons from the inhibited and activated subpopulations whose normalized response and baseline magnitudes significantly decrease, increase, or show no change across trials when mice consumed Ensure under FD or water under WD (as determined by false discovery rate-corrected statistical significance of correlation coefficient). (H) Example neurons during FD from the inhibited subpopulation with response magnitude not correlated (Cell 1) or significantly decreasing (Cell 2) with consecutive Ensure consumption trials. (I) The same as H with example neurons from the inhibited subpopulation during consecutive water consumption trials. (J) Example neurons from the activated subpopulation during water consumption with response magnitude not correlated (Cell 1), significantly increasing (Cell 2) or significantly decreasing (Cell 3). (K) Ensure consumption response of periLC^{VGLUT2} neurons in mice that were *ad libitum* fed or FD on two separate sessions. Black dashed line: first lick. (L) Cumulative distribution of mean scaled ΔF response from all the neurons (left), the inhibited neurons (middle), and the activated neurons (right) in K. (M) The proportion of significantly inhibited, activated or no response neurons when mice consumed Ensure in FD to satiety (S) (top, n = 137, 3 mice) or when mice consumed water in WD to satiety (S) (bottom, n = 142, 3 mice). Statistics: Table S1.

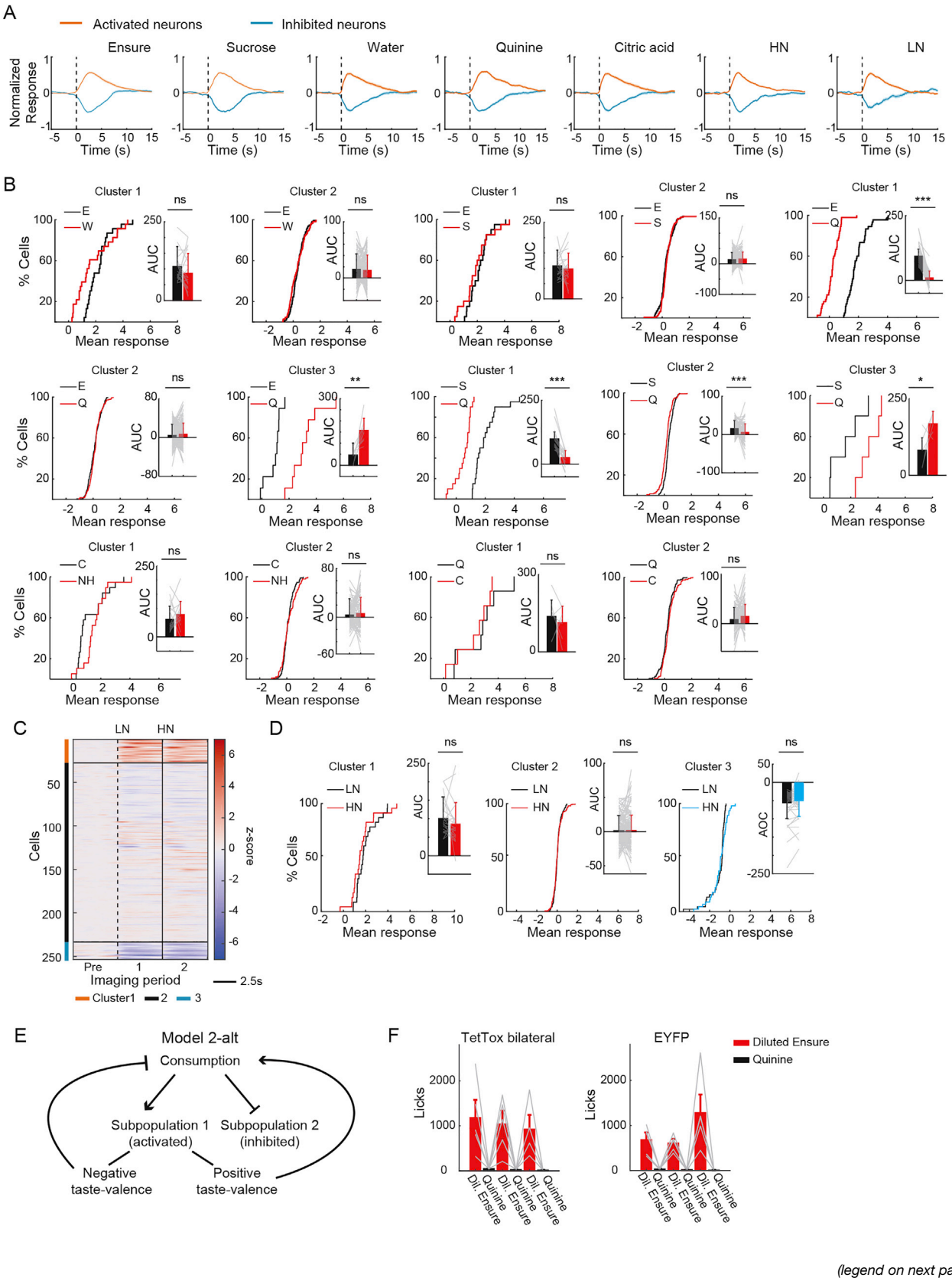

(legend on next page)

Figure S5. PeriLC^{VGLUT2} Neurons Respond to Different Taste Modalities, Related to Figure 5

(A) Mean normalized responses of all the significantly activated or inhibited periLC^{VGLUT2} neurons to different tastants. Blue line: significantly inhibited neurons, orange line: significantly activated neurons. Dashed line: first lick. Shading: ± SEM. (B) Cumulative distribution of the mean z-score responses and the corresponding cell-matched AUC comparison for different clusters shown in Figures 5D–5I. (C) Ensemble response of periLC^{VGLUT2} neurons to low salt (LN) and high salt (HN) grouped by k-means clustering (n = 253 neurons, 3 mice). Dashed line: first lick. Solid vertical line: boundary between LN and HN consumption. Solid horizontal line: division of cell clusters. (D) Cumulative distribution of mean z-score responses and corresponding AUC comparison from each cluster shown in C. E: Ensure; W: water; S: sucrose; Q: quinine; C: citric acid; HN: high salt; LN: low salt. (E) Hypothetical Model 2-alt in which activated subpopulation 1 is divided into negative taste-valence activated neurons and positive taste-valence activated neurons. Potentially, negative-valence activated neurons could inhibit consumption. However, a primary role for these neurons for controlling consumption is not consistent with our finding that inhibition promotes consumption of palatable, non-bitter foods. (F) Cre-dependent tetanus toxin (TetTox) mediated suppression of periLC^{VGLUT2} neurons bilaterally (left, n = 5) did not abolish quinine avoidance compared to EYFP control mice (right, n = 5). Error bars: SD. ns $p > 0.05$, *$p < 0.05$, **$p < 0.01$, ***$p < 0.001$. Statistics: Table S1.

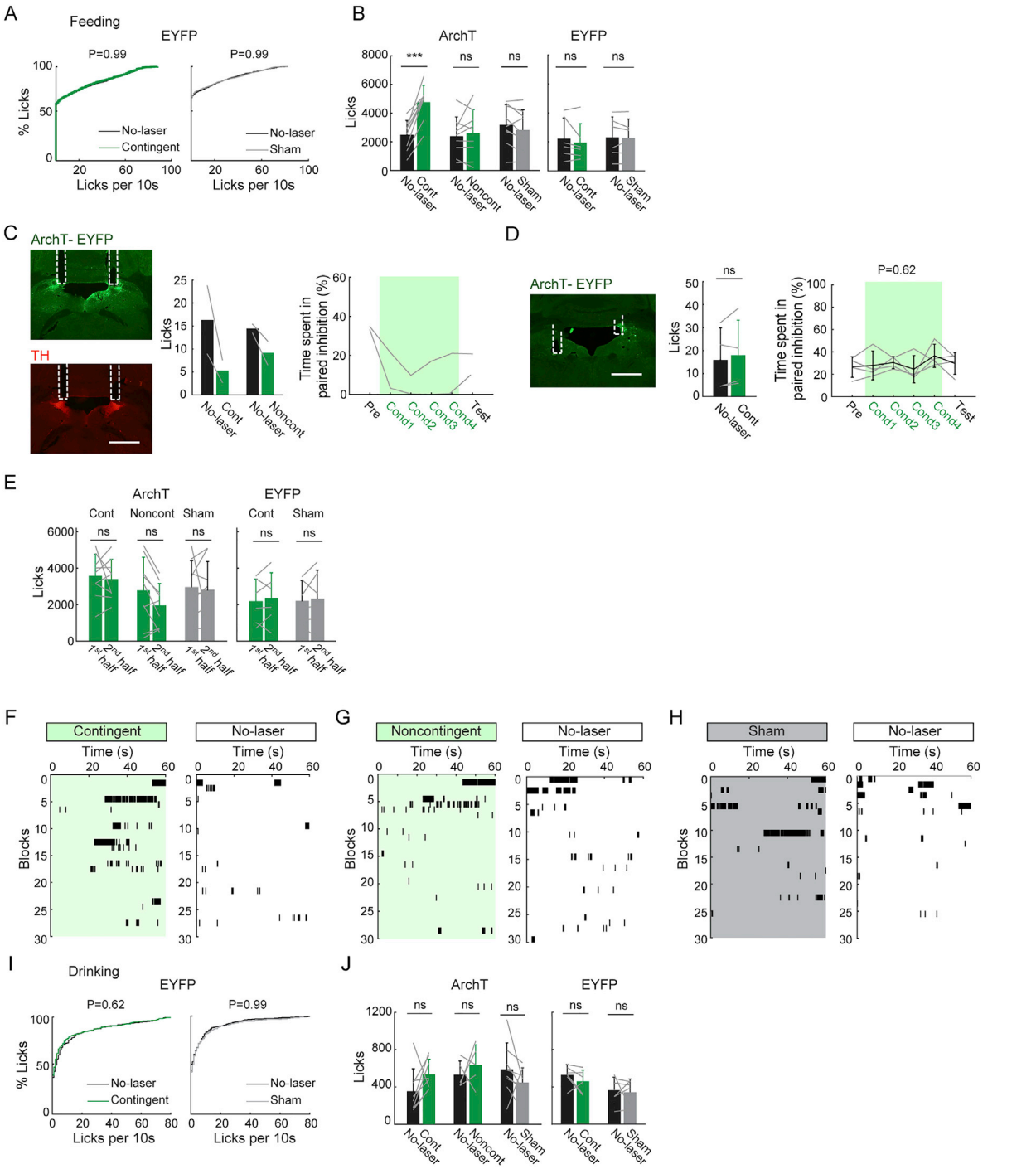

Figure S6. Temporal Control over Consumption, Related to Figure 6

(A) Cumulative distribution of licks analyzed in 10 s bins for EYFP control mice consuming diluted Ensure in the contingent laser-on blocks and no-laser control blocks (n = 6). (B) Total licks for diluted Ensure consumption in contingent, noncontingent, and sham conditions for laser-on and laser-off blocks in periLC^{VGLUT2} ArchT mice and EYFP control mice. (C) Bilateral photoinhibition of VGLUT2 neurons in the caudal LC (TH-IR (red) as anatomical marker) reduced consumption of diluted Ensure and showed place avoidance learning (n = 2). Dashed white rectangle: fiber position. (D) For mice with virus targeting into the fourth ventricle or LDT, no significant changes of diluted Ensure consumption in contingent photoinhibition protocol or in conditioned place preference test (n = 4). (E) Licks in the first and the second half of the sessions under different perturbation paradigms in both ArchT mice and EYFP control mice. (F-H) Lick events for water consumption from a WR ArchT mouse in the contingent (F), noncontingent (G) and sham (H) conditions for laser-on (green) and laser-off (white) blocks. (I and J) As in A and B, for water consumption in WR EYFP control mice (n = 6) and ArchT mice (J, n = 9). Note that lack of statistical significance in total licks for contingent photoinhibition of ArchT mice is related to reduction in bout number (see Figure S7F). Error bar: SD. ns $p > 0.05$, *$p < 0.05$, ***$p < 0.001$ Statistics: Table S1.

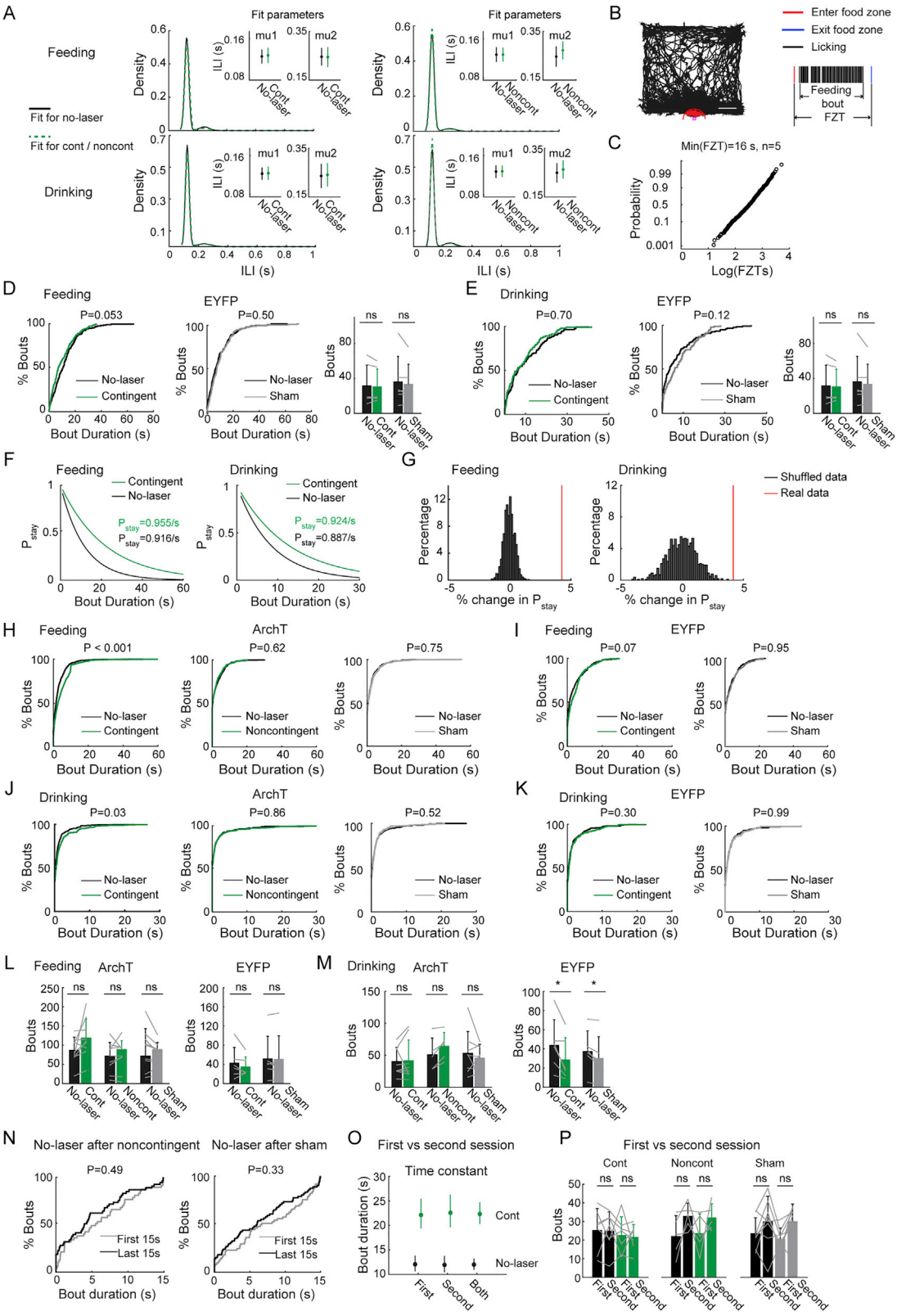

(legend on next page)

Figure S7. Consumption Bout Duration and Initiation during Closed-Loop and Open-Loop Inhibition, Related to Figure 7

(A) Bimodal Gaussian fits to inter-lick intervals (ILIs) that are less than 1 s in the contingent (left) and noncontingent (right) conditions of the laser-on and laser-off blocks during both diluted Ensure consumption (top) and water consumption (bottom). Insets compare the first peak (mu1) and second peak (mu2) of the ILI distributions between contingent (cont) or noncontingent (noncont) and no laser (no-laser) blocks. Error bars are the standard deviations from the fits to the ILIs (sigma1 and sigma2). (B) Locomotion trajectory during one session of closed-loop lick-triggered photoinhibition (left) and an example of sequential behavioral events after a mouse entered the food zone (FZ) (right). Black: locomotion trajectory, Red: mouse position when licking. Red curved line: FZ boundary. FZT: interval between entering and exiting FZ while there is consumption. Scale bar: 5 cm. (C) The minimum FZTs was 16 s. (D) Cumulative distribution of bout duration and total bouts in the contingent and sham conditions of periLC^{VGLUT2} EYFP control mice (n = 6) during diluted Ensure consumption. (E) As in D for water consumption in WR EYFP control mice (n = 6). (F) For illustration purposes, comparison of cumulative probability of staying in a consumption bout calculated at different times based on empirically determined P_{stay} under the contingent inhibition or corresponding no-laser condition for both feeding (left) and drinking (right). (G) Shuffling bouts across all blocks taken from the contingent photoinhibition session and re-partitioning into two groups showed that the ΔP_{stay} under contingent photoinhibition is significantly larger than from the shuffled data for both feeding (left, $p < 0.001$) and drinking (right, $p < 0.001$). See STAR Methods. (H and I) Cumulative distribution of bout duration during diluted Ensure consumption in the contingent, noncontingent, and sham conditions for laser-on and -off blocks when the ILI threshold to define a bout is 1 s in periLC^{VGLUT2} ArchT mice (H) as well as EYFP control mice (I). (J and K) As in H and I for WR mice consuming water. (L) Number of bouts in the contingent, noncontingent and sham conditions when the ILI threshold to define a bout is 1 s during diluted Ensure consumption of periLC^{VGLUT2} ArchT mice and EYFP mice. (M) As in L for water consumption in WR mice. No significant effect on bout number for ArchT mice under any condition. Statistical significance of no-laser versus contingent photostimulation in EYFP mice was observed, but it is also observed for the same mice under sham conditions lacking any laser stimulation, was absent for the 16 s threshold (Figure S7E), was absent for control mice in Figure S7L, and thus was likely a false positive test. (N) Cumulative distribution of bout duration from the initial 15 s and the last 15 s in the no-laser blocks following noncontingent blocks (left) or sham blocks (right) that contain feeding bouts straddling the next no-laser block in periLC^{VGLUT2} ArchT mice. (O) The same as Figure 7H but comparing the results from two consecutive contingent photoinhibition sessions showing bout duration time constant for first, second and both sessions. (P) The same as Figure 7I but with feeding bouts from two consecutive sessions under three perturbation conditions. Error bars: SD. ns $p > 0.05$, *$p < 0.05$. Statistics: Table S1.